

EFD and CFD for KCS heaving and pitching in regular head waves

Claus D. Simonsen · Janne F. Otzen ·
Soizic Joncquez · Frederick Stern

Received: 30 September 2010 / Accepted: 26 March 2013 / Published online: 30 April 2013
© JASNAOE 2013

Abstract The KCS container ship was investigated in calm water and regular head seas by means of EFD and CFD. The experimental study was conducted in FORCE Technology's towing tank in Denmark, and the CFD study was conducted using the URANS codes CFDSHIP-IOWA and Star-CCM+ plus the potential theory code AEGIR. Three speeds were covered and the wave conditions were chosen in order to study the ship's response in waves under resonance and maximum exciting conditions. In the experiment, the heave and pitch motions and the resistance were measured together with wave elevation of the incoming wave. The model test was designed and conducted in order to enable UA assessment of the measured data. The results show that the ship responds strongly when the resonance and maximum exciting conditions are met. With respect to experimental uncertainty, the level for calm water is comparable to PMM uncertainties for maneuvering testing while the level is higher in waves. Concerning the CFD results, the computation shows a very complex and time-varying flow pattern. For the integral quantities, a comparison between EFD and CFD shows that the computed motions and resistance in calm water is in fair agreement with the measurement. In waves, the motions are still in fair agreement with measured data, but larger differences are observed for the resistance. The mean resistance is reasonable, but the first order amplitude of the resistance time history is underpredicted by CFD. Finally,

it seems that the URANS codes are in closer agreement with the measurements compared to the potential theory.

Keywords Seakeeping · CFD · Experiment · Regular head waves · Heave · Pitch · Motions · Added resistance

List of symbols

a_n	n 'th order of amplitude
B_{wl}	Model beam
B_X	Bias limit
C_b	Block coefficient
dt	Time step
D	Distance between carriage wave gauge and LCG
f_e	Frequency of encounter
f_n	Natural frequency
Fn	Froude number
F_X	X force
FS	Fourier series expansion
g	Gravity constant
H	Wave height
I_{yy}	Total moment of inertia of the model
k	Wave number
L_{pp}	Model length between perpendiculars
L_{wl}	Model length of waterline
M	Number of repeats
M_{Model}	Mass of model
p, q, r	Roll, pitch and yaw rate
p_G	Order of accuracy
P_X	Precision limit
Re	Reynolds number
r_G	Grid refinement ratio
R_G	Grid convergence ratio
RM	Running mean
S	Model surface area
S_L	Minimum solution of considered grid

C. D. Simonsen (✉) · J. F. Otzen · S. Joncquez
FORCE Technology, Hjørtækærvej 99, Kongens Lyngby,
Denmark
e-mail: cds@force.dk

F. Stern
IIHR, The University of Iowa, 100 C. Maxwell Stanley
Hydraulics Laboratory, Iowa City, IA, USA

S_r	Standard deviation
S_U	Maximum solution of considered grid
t	Time
T_e	Encounter period
TF_i	Transfer function in i 'th mode
T_m	Model mean draught
T_p	Peak period
u, v, w	Surge, sway and heave velocities
U_0	Model speed
U_C	Carriage velocity
U_G	Grid uncertainty
U_X	Total uncertainty
x_i	i 'th degree of freedom
x, y, z	Axial, transverse and vertical coordinates
X_G	Longitudinal center of gravity (LCG)
X_i	Measured variable
Y	Approximated variable
Y^+	Wall distance
Z_G	Vertical center of gravity (VCG)
$\delta_{RE_{GI}}^*$	Grid error
Δ	Model displacement
Δ_G	Maximum change between grids
Δ_{HSC}	Convergence of RM values
Δ_{SC}	Statistical convergence
ε_{Gij}	Difference between i 'th and j 'th grid
ϕ	Level set function
γ_{Yn}	n 'th order phase
η	Water viscosity
λ	Wave length
∇	Model volume
ρ	Water density
θ	Pitch angle
θ_i	Influence coefficient of i 'th variable
ζ	Surface elevation

1 Introduction

Today, route simulations play an important role for ship owners and operators in order to evaluate the performance of ships sailing on a given route. The performance evaluation is typically focused on determining the average roundtrip duration at a given probability for the voyage duration, but also on calculation of the fuel consumption to determine, for instance, the Ship Energy Efficiency Operational Indicator (EEOI) proposed by the International Maritime Organization (IMO). In order to make realistic simulations, the route simulation tools must, in addition to a wind resistance and propulsion system, also include information about calm water resistance and added resistance due to waves. Typically, the resistance information is

derived from empirical methods, measurements or computations. If computations are used, they are typically based on potential theory methods as discussed in the literature review below. However, the inviscid potential theory methods have limitations so it is of interest to investigate whether more advanced CFD methods like RANS solvers, which include effects like viscosity and turbulence, can be used for the computations. As seen in the literature review below, the application of RANS for this type of calculations is limited. Therefore, the present study is focused on investigating how well RANS simulations work in connection with prediction of added resistance and motions in regular head sea compared to measurements and potential flow computations.

The potential flow theory has been extensively used to calculate the motions and the mean added resistance in waves. In the 1970s, methods based on the strip theory started to appear, such as those of Gerritsma and Beukelman [1] and Salvesen [2]. However, these methods assume that the ship is slender and wall-sided. These limitations could be overcome by the increase of the computer capacity, and consequently the use of three-dimensional panel codes. These codes can be divided into two groups depending on the elementary singularity they use in the boundary integral formulation. In the first group, a transient wave source which satisfies the Kelvin free surface condition is used. This group includes among others the codes WAMIT, TIMIT [3, 4]. These codes can evaluate the motions and the mean added resistance, but only the Neumann–Kelvin linearization is implemented (linearization with respect to the free-stream). The main advantage of these codes is that only the hull needs to be discretized. But the main issue with the codes from this group is the limitation regarding the choice of the free surface condition. Panel codes belonging to the second group use a Rankine source as elementary singularity. This implies that both the hull and free surface need to be discretized. This group includes among others SWAN, SWAN 2 and AEGIR [5, 6]. These codes have proved able to handle complex geometry and to be flexible with the free surface condition.

Despite the extensive work that has been done to improve the accuracy of the codes using potential flow, these codes are still limited by the potential flow theory itself, which does not take into account breaking waves, turbulence or viscosity. One of the alternatives to potential flow theory which can overcome these limitations is the use of RANS (Reynold-Average Navier–Stokes) solvers. As the computers became more powerful, more elaborate turbulent models and larger grids could be used in the calculations. Sato et al. [7] computed ship motions in regular head waves for the Wigley hull, and the Series 60 model. Hochbaum and Vogt [8] simulated a C-Box container ship free to surge, heave and pitch in regular head

waves. The turbulent model was a Wilcox's $k-\omega$ model [9] which meant that two extra equations needed to be solved. Because of the coarse grid that was used, the amplitude of the pitch motion calculated was about 1.5 smaller than the pitch measured. Orihara and Miyata [10] investigated added resistance and pitch and heave motions for an S175 container ship in regular head waves using the Baldwin–Lomax turbulence model. The authors succeeded in showing that the RANS method can capture the difference in added resistance between two bulbous bows. As the RANS method proved to give good results, it was decided to work with increasingly complex geometry and test cases. Weymouth et al. [11] studied pitch and heave for a Wigley hull in regular head waves. Carrica et al. [12] performed simulations for the DTMB model 5512 in regular, small amplitude ($ak = 0.025$) head waves. Hu and Kashiwagi [13] studied pitch and heave motions for a Wigley hull in regular head waves. Stern et al. [14] investigated pitch and heave for BIW-SWATH in regular head waves. Wilson et al. [15] and Paik et al. [16] computed pitch and heave motions of the S175 in regular head waves. Castiglione et al. [17] studied the response of a high speed ($Fr = 0.45, 0.6$ and 0.75) DELFT catamaran in regular head waves. Mousaviraad et al. [18] studied the DTMB 5512 using regular wave and transient wave group procedures. Heave and pitch response amplitudes and phases for the model in head waves were presented. Simonsen and Stern [19] computed the heave, pitch and added resistance for the KCS containership in regular waves for the Gothenburg 2010 CFD workshop, and quite good results were obtained. Finally, Carrica et al. [20] presented irregular wave simulations in connection with extreme ship motions including broaching and surf riding. Based on the above studies, it is found that focus has been placed on motions which are, in general, fairly well predicted. Less attention has, however, been given to resistance, probably because not much data is available from force measurements on ships in waves, especially in oblique seas.

The objective of the present work was to study motions, resistance and flow field for an appended ship sailing in calm water and in regular head seas. The focus was on large amplitude motions, so near resonance and maximum forcing conditions were studied. The work was based on the KCS container ship, shown in Fig. 1, which is one of the benchmark ships within the maneuvering and sea-keeping communities.

The flow was calculated by means of Unsteady Reynolds-Averaged Navier–Stokes (URANS), and the motions of the ship were solved in heave and pitch by a 6 DOF



Fig. 1 KCS container ship geometry

module, which was implemented in the RANS solver. CFDSHIP-IOWA is used for all conditions, while Star-CCM+ is applied to check a single condition. The focus of this paper is on the application of RANS, but results from the potential theory time domain code AEGIR are included in order to see how potential theory results compare with the RANS results. Complementary towing-tank resistance tests in calm water and in waves were conducted for validation purposes. The test included an uncertainty assessment. Further, the measured data was also used as a test case at the Gothenburg 2010 CFD workshop.

The approach for the research was to study the flow problem in a stepwise manner. Based on Experimental Fluid Dynamics (EFD) and Computational Fluid Dynamics (CFD), the work covered the following: (1) study of the ship sailing in calm water, (2) study of the ship sailing in regular head seas, (3) comparison of results from conditions (1) and (2) including calculation of the added resistance in waves, and (4) verification of the CFD tools and validation against measured data. In the study, the ship was equipped with a rudder, but the propeller was not included.

The article is organized as follows. After a description of the geometry and conditions, the applied methods and approaches are described, i.e. experimental setup and uncertainty assessment method plus computational method. After this, the results are discussed. First the experimental results are covered to explain the measurement uncertainties and the trends in the data. Second, the CFD results are covered to explain verification of the method, flow physics and how well the computations agree with the measurements. Finally, conclusions and recommendations for future activities are given.

2 Geometry and conditions

The appended hull of the 230 m KCS container ship, Fig. 1, is considered in the model scale 1:52.667. The main particulars of the ship are listed in Table 1.

Table 1 Main particulars of KCS model

L_{PP}	m	4.367
L_{WL}	m	4.414
B_{WL}	m	0.611
T_m	m	0.205
∇	m ³	0.356
Δ	Ton	0.356
S	m ³	3.436
C_b	–	0.651
I_{yy}	kg m ²	336.34
* X_G	m	–0.065
* Z_G	m	–0.067

* Indicates location of COG in (X^* , Z^*) coordinates. See Fig. 2

Speeds and wave parameters have been chosen in order to study large amplitude motions and conditions near resonance and with maximum excitation based on the findings in Irvine et al. [21]. If the behavior of the pitching and heaving ship is described in analogy to a mass-spring-damper system with forced motions, two things influence the response of the ship. One is resonance, and the other is the size of the exciting loads. Resonance occurs if the system is excited with a frequency equal or close to the natural frequency f_n of the system. In this case, even small excitation forces will result in a large response. In connection with ships, the excitation frequency is determined by the frequency of encounter of the waves, $f_e = \sqrt{g/(2\pi\lambda)} + U_0/\lambda$ which means that excitation frequency depends on the ship speed U_0 and the wave length λ . When it comes to the exciting forces and moments, they originate from the passing wave. The excitation forces and moments depend on the wave and ship lengths, and according to strip theory, the maximum caused by the exciting loads seems to occur for wave lengths close to $\lambda/L_{pp} = 1.33$.

If the condition $f_e = f_n$ is met for a specific speed, it does not necessarily happen for a wave length satisfying $\lambda/L_{pp} = 1.33$. Irvine et al. [21] suggests that the maximum response of the ship will occur when the above conditions are satisfied at the same time, i.e. when $f_e = f_n$ and $\lambda/L_{pp} = 1.33$ coincide in the same condition. But in the work by Irvine et al. [21], the conditions for maximum heave and maximum pitch excitation forces and moments were not distinguished, and $\lambda/L_{pp} = 1.33$ were used for both heave and pitch. In Sadat-Hosseini et al. [22], it has been verified that the surge and pitch excitation forces are largest around $\lambda/L_{pp} = 1.33$, whereas the heave excitation force increases by increasing wave length.

If the conditions $f_e = f_n$ and $\lambda/L_{pp} = 1.33$ are used in the expression for the encounter frequency, it is possible to find the speed where the response should have its maximum with regard to pitch and surge. For heave force and heave motion, the maximum will shift with the ship speed as suggested in Sadat-Hosseini et al. [22], i.e. the peak will occur in long waves and near resonance condition which shifts to longer wave regions with increasing ship speed.

The test program in Table 2 is designed to study the ship's maximum response in waves, and the speeds are chosen to investigate the maximum response idea described above, i.e. investigate conditions near $f_e = f_n$ and $\lambda/L_{pp} = 1.33$, disregarding the discrepancy with regard to heave for which the maximum region depends on the speed and not $\lambda/L_{pp} = 1.33$. For the present model, the natural frequencies in heave and pitch are estimated to be close to $f_n \approx 0.9$ Hz. The estimate of the natural frequencies is based on $\omega_5 = \sqrt{C_{55}/(I_{55} + A_{55})}$ and $\omega_3 = \sqrt{C_{33}/(m + A_{33})}$ from [21]. $C_{55} = \rho g I_T$ and $C_{33} = \rho g A_W$ are the restoring pitch moment

Table 2 Model test program for resistance tests in calm water and in waves

Test in regular head waves				
Froude number	Wave/ship length	Steepness H/λ	Height H (m)	Encounter frequency (Hz)
0.26*	–	–	No waves	
0.26	0.28	1/60	0.020	2.52
0.26	0.44	1/60	0.032	1.79
0.26	0.50	1/60	0.036	1.63
0.26	0.71	1/60	0.052	1.26
0.26*	1.15	1/60	0.084	0.90
0.26	1.33	1/60	0.097	0.81
0.26	1.50	1/60	0.109	0.75
0.26	2.00	1/60	0.146	0.62
0.33	–	–	No waves	
0.33	0.50	1/60	0.036	1.83
0.33	1.15	1/60	0.084	0.99
0.33	1.33	1/60	0.097	0.89
0.33	1.50	1/60	0.109	0.82
0.33	2.00	1/60	0.146	0.67
0.40	–	–	No waves	
0.40	0.50	1/60	0.036	2.04
0.40	1.15	1/60	0.084	1.08
0.40	1.33	1/60	0.097	0.97
0.40	1.50	1/60	0.109	0.89
0.40	2.00	1/60	0.146	0.72

* Indicates repeated tests

and heave force, respectively. I_T and A_W are the moment of inertia and the area of the water plane. Further, I_{55} and m are the mass moment of inertia around the Y axis and the mass of the ship. Finally, the added mass and added moment of inertia can be approximated with $A_{33} \approx m$ and $A_{55} \approx I_{55}$, respectively. Three model speeds are considered: $U_0 = 1.701$ m/s, $U_0 = 2.138$ m/s and $U_0 = 2.603$ m/s which correspond to 24.0, 30.2 and 36.7 knots in full scale. The Froude number, $Fn = U_0/\sqrt{gL_{pp}}$, where U_0 is the ship speed, g is the gravitational constant and L_{pp} ship length, is seen in Table 2. The model Reynolds number, $Re = U_0 L_{pp}/\nu$ where ν is the kinematic viscosity of the water equals $Re = 6.517 \times 10^6$, $Re = 8.190 \times 10^6$ and $Re = 9.971 \times 10^6$.

The speed $U_0 = 1.701$ m/s corresponds to the ship's service speed. The two remaining speeds may be unrealistically high seen from a practical point of view, but they were chosen in order to study the above maximum response idea. The $f_e = f_n$ and $\lambda/L_{pp} = 1.33$ conditions are written in bold in the table. At low speed, resonance occurs at a wave length shorter than $\lambda/L_{pp} = 1.33$. At medium speed, the two conditions coincide, and at high speed, the wave length is higher than $\lambda/L_{pp} = 1.33$ when resonance occurs.

For all considered speeds, both calm water and regular head wave conditions are considered in order to extract information about the added resistance in waves.

Further, in order to assess the experimental uncertainty for future CFD validation, the test program contains repeated tests for a few conditions. These conditions are marked with (*) in Table 2. The applied uncertainty analysis (UA) procedure is described below. The CFD conditions considered in the present work are written in bold in Table 2. This means that a total of eight calculations have been conducted.

It should be noted that in addition to the tests in Table 2 with steepness $H/\lambda = 1/60$, tests with steeper waves and with the propeller running behind the ship were made. However, for the present presentation, the steepness and propeller studies are left for future activities. All conditions are documented in Otzen and Simonsen [23].

3 Experimental method, test setup and UA procedure

3.1 Facility

The model tests were conducted in the deep water towing tank at FORCE Technology. The tank is 240 m long, 12 m wide and 5.5 m deep, and equipped with a wave maker in one end and a wave dampening beach at the opposite end. The computer controlled hydraulic double flap wave maker is capable of generating regular or irregular waves with a range of $T_p = 0.5 - 7$ s and maximum height of 0.9 m.

3.2 Model test setup

The model was attached underneath the carriage by two trim holders and restrained in surge, sway and yaw. The model was fixed with zero heel and drift angles, i.e. the effect of static heel and yaw was not considered. Consequently these degrees of freedom are not included in the uncertainty analysis described in Otzen and Simonsen [23].

The model was ballasted on the basis of the marks. To position the ballast weights achieving the target values for the vertical center of gravity (VCG), longitudinal center of gravity (LCG) and radius of inertia, the pendulum method was applied. It is an incline test in air where the model including gauges is placed on a set of knife-edges to find the radius of inertia and VCG of the hull.

$$I_{yy, \text{Model}} = M_{\text{Model}} \left(\left(\frac{T_{yy}}{2\pi} \right)^2 g |OG| - |OG|^2 \right) \quad (1)$$

$$|OG| = \frac{V}{M_{\text{Model}}} \frac{1}{a} (n^2 + a^2) \quad (2)$$

where T_{yy} is the mean period of the free pitch motion, $|OG|$ is the distance from the knife-edges to VCG, and M_{Model} is model weight including gauges. To determine $|OG|$, a small weight V is displaced at the distance n from LCG resulting in a vertical displacement a of the point at AP horizontal in line with the knife-edges. Afterwards, the final contribution required from the ballast weights can be evaluated based on position and mass to achieve the final values for radius of inertia and VCG of the model. In all tests, the rudder was locked at an angle of zero degrees. During the resistance tests, the stern tube at the propeller bossing was closed with a streamlined cap.

3.3 Data acquisition

Data acquisition was made for each run for all the quantities listed in Table 3. All data was acquired as time series using a sampling frequency of 45 Hz. The time series were recorded when the carriage had reached steady velocity, i.e. zero carriage acceleration was assumed during the runs.

The equipment used to measure quantities 1–7 and 9 was all positioned on the carriage or model. Quantities 2, 3, 6 and 7 were measured in the ship coordinate system (x' , z') illustrated in Fig. 2, whereas the X-force and the carriage velocity were measured in the global coordinate system. The X-force was measured by two gauges. The stationary wave probe was positioned alongside the tank 30 m from the wave maker.

From the measured quantities, a number of additional channels were derived as listed in Table 4. Detailed descriptions of the data reduction equations for the derived channels are available in Otzen and Simonsen [23].

Table 3 Overview of measured quantities

		Quantity	Unit
1	U_c	Speed	m/s
2–3	$z_{\text{for}}, z_{\text{aft}}$	Sinkage, for and after	mm
4–5	$F_{X, \text{for}}, F_{X, \text{aft}}$	X-Force, for and aft	N
6–7	$\dot{w}_{\text{aft}}, \dot{w}_{\text{aft}}$	Acceleration at FP and AP	m/s ²
8	ζ_s	Wave, stationary probe	m
9	ζ_e	Wave of encounter	m

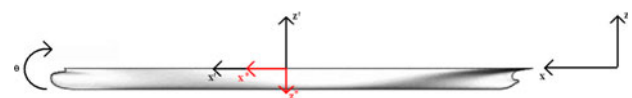


Fig. 2 Applied coordinate system in measurement

Table 4 Overview of derived quantities

		Quantity	Unit
1	\dot{w}	Acceleration midship	m/s ²
2	z	Heave, midship	m
3	F_X	Total X-force	N
4	w	Vertical velocity	m/s
5	θ	Pitch	deg
6	q	Pitch rate	deg/s
7	\dot{q}	Pitch acceleration	deg/s ²

3.4 Data reduction equations

For the calm water tests, the measured X-force is non-dimensionalized, and so X' becomes

$$X' = \frac{F_{X,\text{meas}}}{0.5\rho U_C^2 S} \quad (3)$$

where $F_{X,\text{meas}}$ is the X-force measured in the global coordinate system, ρ is the water density, S is the wetted surface area, and U_C is the ship or carriage speed.

For wave conditions, the time series for the raw measured quantities, i.e. the force $F_{X,\text{meas}}$, the wave elevation and the heave and pitch motions, were approximated with Fourier series expansions (FS) as

$$Y_{\text{FS}}(t) = a_0 + a_1 \cos(2\pi f_e t + \gamma_{Y1}) + a_2 \cos(4\pi f_e t + \gamma_{Y2}) + a_3 \cos(6\pi f_e t + \gamma_{Y3}) \quad (4)$$

where Y represents the approximated variable, a_n is the n th order amplitude, and γ_{Yn} is the n th order phase. Three orders were used in the FS reconstruction to analyze linearity and correlation between the encounter wave and the excited forces and motions. In connection with the added resistance, the excited force was analyzed by first subtracting the calm water resistance. Afterwards it was non-dimensionalized with the 1st harmonic wave amplitude and the ship length L_{PP} and beam B instead of ship speed and surface area as in Eq. 3, where the data reduction equation becomes

$$\sigma_{\text{aw}} = \frac{(F_{X,\text{meas}} - F_{X,\text{meas,calm}})}{\rho g \zeta_{I1}^2 B^2 / L_{PP}}. \quad (5)$$

In connection with studies of the absolute resistance $F_{X,\text{meas}}$ for the ship sailing in waves, the non-dimensionalization in (3) was applied. The disadvantage of this method is that it does not remove the effect of possible different wave heights used in the experiment and the CFD simulation, but it was used anyway.

The motions were analyzed with transfer functions (data reduction equations) given by

$$\text{TF}_{x3} = \frac{x_{3I}}{\zeta_{I1}} \quad (6)$$

$$\text{TF}_{x5} = \frac{x_{5I}}{k\zeta_{I1}} \quad (7)$$

where x_{3I} , x_{5I} and ζ_{I1} are the 1st harmonic amplitudes of heave, pitch and head wave time history, respectively, and $k = 2\pi/\lambda$ is the wave number. The phases were calculated by means of

$$\gamma_{\text{LCG}} = \gamma_{\zeta_{I1}} - 2\pi \frac{D}{\lambda} \quad (8)$$

where $\gamma_{\zeta_{I1}}$ is the 1st harmonic phase of the regular head wave at the carriage wave gauge, D is the distance between the carriage wave gauge and LCG. To evaluate the phase relation, γ_{LCG} is forced into a range of $\pm\pi$ and then subtracted from the 1st harmonic phases of the motions, heave and pitch, and the forces

$$\gamma_Y = \gamma_{\text{LCG}} - \gamma_{YI}. \quad (9)$$

Thereby the heave and pitch phases are expressed as if the time histories were acquired when a wave crest coincides with the LCG at $t = 0$.

3.5 Statistical convergence

Statistical convergence of $F_{X,\text{meas}}$, x_3 and x_5 are estimated based on two approaches. Approach I is based on the convergence of the running mean (RM) values with the amplitude U_{SC} . U_{SC} is defined as half the difference Δ_{SC} between the local maxima and minima of RM. Approach II is based on Yoon [24]. Here, the convergence of FS harmonic amplitude H is estimated. The time history of H is found by applying FS on a window of the time series covering a single period, and then stepping the window throughout the time series.

The convergence of H is then estimated based on the convergence of RM values with amplitude U_{HSC} similarly to U_{SC} . The average of the last U_{SC} and U_{HSC} for the repeated resistance run in waves (see Table 2) is presented in Table 8. As convergence criteria, the amplitudes ought to be smaller than the measurement uncertainty U_X . This criterion is seen to comply for both U_{SC} and U_{HSC} . Finally, it should be noted that the statistical convergence is only used to check the time series. It is not included as an uncertainty source since the precision limit is assumed to include this effect.

3.6 UA approach: data reduction equations

The present uncertainty assessment for the seakeeping test is based on the following procedures: the work done in Irvine et al. [21] and ITTC [25]. The uncertainty analysis

(UA) is applied to the data reduction Eqs. 3, 6 and 7, i.e. considering both the static (calm water) and dynamic (in waves) test cases. For the present paper, focus is placed on uncertainty results for the force Eq. 3 for which both precision and bias limits are estimated. Details of the motion uncertainties are found in Otzen and Simonsen [23]. Doing UA for the data reduction Eq. 5 for the added resistance was not within the scope of the work.

3.6.1 Total uncertainty

The total uncertainty for the average X is given by

$$U_{\bar{X}}^2 = B_{\bar{X}}^2 + P_{\bar{X}}^2 \quad (10)$$

where B_X and P_X are the bias and precision limits, respectively.

3.6.2 Bias limits

The bias limits were assessed based on a study of the measuring system and computed according to ITTC 1999a [25]

$$B_r^2 = \sum_{i=1}^J \theta_i^2 B_i^2 + 2 \sum_{i=1}^{J-1} \sum_{k=i+1}^J \theta_i \theta_k B_{ik} \quad (11)$$

where θ_i is the influence coefficient defined by

$$\theta_i = \frac{\partial r}{\partial X_i} \quad (12)$$

B_i is the elemental bias limit in X_i , and B_{ik} is the correlated bias limit in X_i and X_k .

$$B_{ik} = \sum_{\alpha=1}^L (B_i)_\alpha (B_k)_\alpha \quad (13)$$

where L is the number of correlated bias error sources that are common for measurement of variables X_i and X_k .

The bias error for each variable in the data reduction equation may consist of a number of bias errors, so in order to calculate the combined bias error, the root-sum-square is used

$$B_i^2 = \sum_{k=1}^J (B_i)_k^2 \quad (14)$$

where i is the number of the considered variable in the data reduction equation.

3.6.3 Precision limits

The precision limits are assessed through repeated tests. Since the model was not dismantled during the test, the repeat tests were mixed into the test program in order to

“disturb” the system. The precision limits were computed according to ITTC [25]

$$P_{\bar{r}} = \frac{2S_{\bar{X}}}{\sqrt{M}} \quad (15)$$

where M is the number of repeats, and the factor of 2 was applied for $M \geq 10$. S_X is the standard deviation defined as

$$S_{\bar{X}} = \left[\sum_{k=1}^M \frac{(X_k - \bar{X})^2}{M-1} \right]^{1/2} \quad (16)$$

Here, X_k is the value from each repeat test, and \bar{X} is the mean value of all the quantities from the repeat tests. \bar{X} is defined as

$$\bar{X} = \frac{1}{M} \sum_{k=1}^M X_k. \quad (17)$$

It should be noted that for the static test, all the quantities in the expressions above are time averaged and as such constant. But in the dynamic tests, they are all varying in time. This means that the expressions are being applied on sets of data from the time series which are taken at fixed times throughout the encounter wave cycle, i.e. at $t = 0, t_1, t_2, \dots, t_{\text{period}}$. The time step applied in the present work is 0.0222 s.

3.6.4 Bias estimates

The bias limits are computed for all variables in the data reduction equations by applying error propagation Eqs. 11–14 to data described in Eqs. 3, 6 and 7. Assuming none of the variables are correlated, the bias limit equation for X' is given by

$$B_{X'}^2 = \theta_{F_{X,\text{meas}}}^2 B_{F_{X,\text{meas}}}^2 + \theta_{\rho}^2 B_{\rho}^2 + \theta_S^2 B_S^2 + \theta_{U_C}^2 B_{U_C}^2. \quad (18)$$

The bias limits for the 1st order amplitudes of heave x_3 and pitch x_5 are given by

$$B_{x3}^2 = \theta_{x3}^2 B_{x3}^2 + \theta_{\zeta}^2 B_{\zeta}^2 \quad (19)$$

$$B_{x5}^2 = \theta_{x5}^2 B_{x5}^2 + \theta_{\zeta}^2 B_{\zeta}^2 + \theta_k^2 B_k^2. \quad (20)$$

The influence coefficients θ are derived by applying Eq. 12 on the data reduction Eq. 3 for the force and 6 and 7 for the motions. The elemental bias limits B are the uncertainty related to the applied measurement equipment and are determined with independent tests.

3.6.5 Elemental bias errors

As an example of the elemental bias limit calculations, the bias limit of the measured force, $F_{X,\text{meas}}$, is assumed to consist of four components:

- calibration of the force gauges
- data acquisition
- encounter surface elevation
- time

where the error contribution of each component is determined with individual tests.

$$B_{F_X, \text{meas}} = \sqrt{B_{\text{calib}, F_X, \text{meas}}^2 + B_{\text{acquis}, F_X, \text{meas}}^2 + B_{\zeta_e, F_X, \text{meas}}^2 + B_{t, F_X, \text{meas}}^2}. \quad (21)$$

As an example, the bias limit of the force related to the surface elevation of the encounter wave is determined as

$$B_{\zeta_e, F_X, \text{meas}} = \frac{\partial F_X, \text{meas}}{\partial \zeta_e} \varepsilon_{\zeta_e}. \quad (22)$$

The influence coefficient is simply found by differentiating the force with respect to the surface elevation and then multiplying the uncertainty of the surface elevation determined from individual tests to evaluate the total contribution.

Besides the uncertainty in the surface elevation which was used to evaluate the bias limits for the motions and resistance, the uncertainty of the separate wave parameters such as length, period, etc. was also investigated in order to evaluate the repeatability of a single wave and to map the decay of the wave throughout the tank.

The decay throughout the tank was evaluated as the slope of the difference between the stationary and the mobile wave gauges as a function of the distance from the wave maker. The error due to decay of the wave was smeared out over the entire logging distance, using a constant error approach as applied in the ITTC guidelines.

A detailed description of the applied procedures and the considered error sources can be found in Otzen and Simonsen [23].

4 Computational method, grids, simulated conditions and verification approach

The computations were performed with the CFD code CFDSHIP-IOWA. The code is an unsteady general-purpose, multiblock, parallel computing URANS code which models the free surface by the single-phase level set method. The code solves the non-dimensional continuity and unsteady RANS equations which are derived and solved in absolute inertial earth-fixed coordinates (x, y, z) for an arbitrary moving and non-deforming control volume and solution domain, respectively (see Fig. 3). Using this approach, the local grid velocity is introduced which again makes implementation of boundary conditions simpler compared to solving the momentum equations in a non-inertial ship-fixed coordinate system, and at the same time

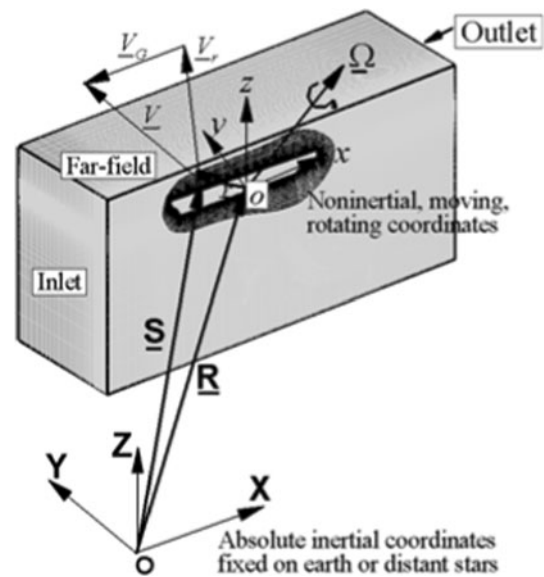


Fig. 3 Definition of absolute inertial earth-fixed coordinates (X, Y, Z) and non-inertial ship-fixed coordinates (x, y, z)

it helps in reducing the computational cost since the computational domain moves along with the body and therefore only has to be large enough to resolve the flow in a limited region around the ship.

The method works in the following way: the flow field is solved, and the forces and moments acting on the ship are calculated in the earth-fixed coordinate system. Then the forces and moments are transformed into a non-inertial ship-fixed coordinate system which has its origin O in the ship's center of gravity. Here the equations of motion are solved to find the ship's translational and angular velocities. These velocities are then transformed back to the earth-fixed coordinate system where they are integrated to find the new position of the ship and grid system. The complete grid system is moved after each time step. However, due to the iterative solution procedure, positions are corrected during the inner iterations on each time step until convergence of the motion is obtained. For the present simulation, a minimum of five inner iterations are applied on each time step. The non-dimensional time step is set to $\Delta t = 0.005$ which gives 85 time steps per period of encounter. Time is non-dimensionalized as tU_0/L_{pp} . For turbulence modeling, the code applies the isotropic blended $k-\omega/k-\varepsilon$ SST model without wall functions. The code is discretized by means of finite differences and applies 2nd order upwind differences for convective terms and central differences for diffusive terms. The temporal discretization is done with a 2nd order backward difference scheme. The pressure and velocities are coupled by means of the PISO (Pressure Implicit with Splitting of Operators) method. Finally, it should be noted that before the governing equations are solved, they are non-dimensionalized with

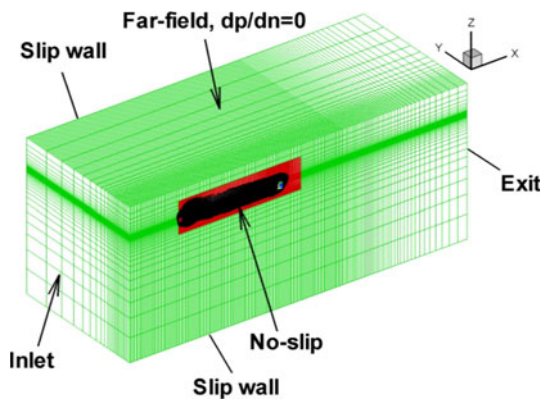


Fig. 4 Chimera Grid applied in CFDShip-IOWA. Only starboard side mesh is shown

Table 5 Block dimensions for applied grid

Block	Dimension
Boundary layer, hull	$401 \times 46 \times 109$
Hull-rudder junction	$173 \times 32 \times 25$
Main rudder	$173 \times 32 \times 80$
Rudder tip	$100 \times 32 \times 51$
Propeller 1	$35 \times 35 \times 99$
Propeller 2	$40 \times 35 \times 35$
Background 1	$204 \times 48 \times 76$
Background 2	$233 \times 48 \times 61$
Total	4,351,785

U_0 , ρ , μ and L_{pp} and then transformed into non-orthogonal curvilinear coordinates. A detailed description of the computational method and the governing equations is found in Carrica et al. [12] and Xing et al. [26].

With respect to gridding approach, the code uses overset multiblock chimera grids which are generated with the software Gridgen and dynamically overset with Suggar, Noack [27]. The grid applied in the present CFD calculations consists of eight blocks, as seen in Fig. 4 and Table 5. In Table 5, two propeller blocks are listed. These blocks do not represent the propeller geometry but are simply refined cylindrical regions which were included for later body-force propeller calculations. In the wave zone, approximately 100 points were used per wavelength in front of and along the ship. In the vertical direction, 10 points were used over the wave height.

As mentioned earlier, the computational domain moves with the ship in the inertial earth-fixed coordinate system. For this particular application where the ship is free to heave and pitch in the waves, different parts of the domain moves with different degrees of freedom. Basically all the blocks are translated with the ship in surge. But in addition to this, the ship, rudder and propeller domains (black and

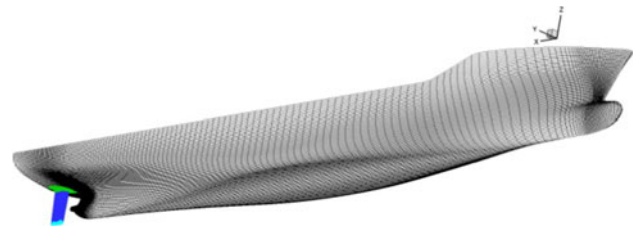


Fig. 5 Surface mesh on hull and rudder

blue regions in Fig. 4) are moving in heave and pitch to capture the wave-induced motions. By doing this, it is possible to maintain the fine grid resolution of the background grids in the wave region which is necessary to carry the wave through the computational domain without too much dissipation.

Concerning the boundary conditions, a no-slip condition was applied on the hull and rudder surfaces, as in Fig. 5. The velocity on these surfaces corresponds to the calculated velocity of the ship. For instance if the ship sails straight ahead with speed U_0 , the boundary condition would be $(u, v, w) = (U_0, 0, 0)$. Due to application of turbulence modelling without wall functions, the near wall spacing was designed so that the wall distance equals $Y^+ \approx 1$.

The outer boundaries upstream, next to and behind the ship were located within distances of approximately 0.6, 1.5 and 2.0 ship lengths from the ship, respectively. The width and depth of the domain were chosen so that they matched the dimension of the towing tank where the data for validation was measured, and the origin of x was shifted to amidships ($L_{pp}/2$) correspondingly, see section about EFD above. Upstream of the ship, an inlet boundary condition describing the regular incoming wave was applied in order to prescribe the wave elevation ζ , the inlet velocities (u, v, w) and the pressure p . The expressions describing the wave are shown below. They are non-dimensionalized in the same way as used in the RANS code, i.e. positions are non-dimensionalized with ship length, velocities with ship speed and pressure with ship speed and water density as described above. The $1/2$ subtracted from x originates from the x shift of $L_{pp}/2$ described above. The wave was prescribed using linear potential flow theory, which is commonly done for RANS calculations with regular waves. However, due to real-fluid effects in the RANS method and the steepness of the applied waves, the non-linear effects are non-negligible and will make the wave crest slightly sharper and taller and the troughs slightly wider and shallower as the wave travels forward from the inlet boundary, similar to what happens in the towing tank when imposing linear waves. It could be considered to include non-linear terms of the wave as described by Stokes [28] to test how the results would be influenced. Doing this was not within

the scope of the present work, but could be considered in future work.

$$\zeta_I(x, t) = a \cos[k(x - 1/2) - 2\pi f_e t] \quad (23)$$

$$u(x, y, z, t) = U_0 + \frac{a}{Fn} \sqrt{k} e^{kz} \cos[k(x - 1/2) - 2\pi f_e t] \quad (24)$$

$$v(x, y, z, t) = 0 \quad (25)$$

$$w(x, y, z, t) = \frac{a}{Fn} \sqrt{k} e^{kz} \sin[k(x - 1/2) - 2\pi f_e t] \quad (26)$$

$$p(x, y, z, t) = \frac{a}{Fn^2} e^{kz} \left\{ \cos[k(x - 1/2) - 2\pi f_e t] - \frac{1}{2} \frac{a}{k} e^{kz} \right\} \quad (27)$$

The level set function on the inlet boundary is set by

$$\phi(x_i, t) = \zeta_I(x_i, t) - z(x_i). \quad (28)$$

Finally, free stream turbulence for k and ω is set to 10^{-7} and 9, respectively.

On the sides and on the bottom of the domain, an impermeable slip surface condition was applied. Using this boundary condition prevented the water from flowing through the domain which was also the case in the towing tank. All other variables had zero gradient conditions. Due to the slip condition, the water did not “stick” to the wall as it does in the towing tank. However, with the relatively large distance between ship and outer boundaries, a possible wall boundary layer due to blockage-driven acceleration of the flow was negligible. Behind the ship, a zero-gradient exit condition was applied for all variables, and finally on the top of the domain, a zero pressure gradient condition was applied.

Star-CCM+ is a commercial URANS code, which is a finite volume code. Free surface is modeled with the volume of fluid method and turbulence with the k - ω model. Setup of this simulation is similar to the one used for CFDSHIP-IOWA, except for the meshing approach, where Star-CCM+ applies sliding interfaces between hull boundary layer mesh and background grid instead of overset meshes in order to capture the pitch motion. A detailed description of the method is found in the Users Manual [29] for the code.

The results obtained in waves were compared with results given by AEGIR [30]. AEGIR is a three-dimensional B-spline based boundary element code. It uses the Rankine source as the elementary singularity. Contrary to Star-CCM+ or CFDSHIP-IOWA, AEGIR is a potential theory code.

As shown in Table 2, the experimental program covers quite a few conditions. A limited set consisting of eight conditions was selected for CFD: three in calm water and five in waves. These conditions are marked in bold in the table. The condition with $Fr = 0.26$, $f_e = f_n = 0.9$ Hz and

$\lambda/L_{pp} = 1.15$ is the one used for Verification and Validation (V&V). The reason is that this particular condition was used in connection with rigorous experimental uncertain assessment during the model test was in order to estimate both bias and precision limits. In relation to the verification, it should be noted that the experiment was conducted with the model equipped with a rudder. But, when the grid study was conducted, it turned out that it was not possible to obtain valid interpolation stencils for the overlapping meshes in the rudder region for the coarser grids so the verification was done without the rudder. However, for the simulation error estimates on the global motion and force levels, the bare hull model is assumed to give results that are representative for the appended hull case. The verification study used three systematically refined grids. When choosing the grid refinement ratio, there had to be a balance between not making the fine mesh too fine due to limitations on computer resources and not making the coarse mesh too coarse and ending up with a coarse mesh on which the solution would be unobtainable or unacceptably resolved, particularly since the present problem involves overset meshes, waves and large amplitude motions which are difficult to handle on very coarse grids. Based on this, a refinement ratio equal to $\sqrt[4]{2}$ was applied. It may not be the optimal value since small refinement ratios give small solution changes which can be difficult to handle when it comes to estimating the grid errors as illustrated later. However, it was the ratio possible within the given limitations and has been used previously in our own and other researchers' verification studies. Of the 26 submissions for the four seakeeping test cases at the Gothenburg 2010 CDF Workshop, only two performed verification studies including the present study, which indicates the difficulty of performing verification for seakeeping applications.

Based on $r_G = \sqrt[4]{2}$ and a fine grid consisting of five blocks and 3,768,044 points, the applied medium and coarse grids ended up having 2,502,605 and 1,762,189 points, respectively. It should be noted that the background grid was not changed in order to be able to carry the wave through the domain, consequently all three grids used the fine background grid.

In order to verify the computational method, the uncertainty related to the numerical method must be estimated. In the present work, the following effects were investigated: statistical convergence, time step, sensitivity to location of the vertical position of the center of gravity and grid size. The statistical convergence was investigated based on running means of the time series while sensitivity of time step and center of gravity were studied based on small changes in these quantities. An approach for estimating the grid uncertainty U_G is presented in Stern et al.

[31], Wilson et al. [32] and Xing and Stern [33]. U_G is estimated based on three systematically refined grids, and factors of safety are used to include the proximity to the asymptotic range in the estimate. Briefly, the procedure is as follows. The changes in solutions between coarse and medium grids, $\varepsilon_{G32} = S_3 - S_2$, and between medium and fine grids, $\varepsilon_{G21} = S_2 - S_1$, are used to calculate the convergence ratio $R_G = \varepsilon_{G21}/\varepsilon_{G32}$. Depending on the value of R_G , three conditions can occur: (i) $0 < R_G < 1$, grid convergence, (ii) $R_G < 0$, oscillatory convergence and (iii) $1 < R_G$, grid divergence. In condition (iii), no uncertainty can be estimated. In condition (ii) the uncertainty is estimated by

$$U_G = |1/2(S_U - S_L)| = |1/2\Delta_G| \quad (29)$$

where S_U and S_L are the maximum and minimum of the solutions from the considered grids. In condition (i), grid convergence occurs, and generalized Richardson extrapolation (RE) is used to estimate the grid error $\delta_{\text{REG1}}^{*(1)}$ and the order of accuracy p_G . In order for the method to be applied, the grids must be related to each other in a systematic way, i.e. the grid refinement factor r_G must be the same between coarse and medium grids and medium and fine grids:

$$r_G = \Delta x_{G2}/\Delta x_{G1} = \Delta x_{G3}/\Delta x_{G2} \quad (30)$$

The computations covered in the present work were unsteady, which means that forces and motions are presented as time series. In order to estimate the grid uncertainty, the above approach was applied to the considered quantity at each time step, for instance if F_X is calculated at $t = 0$, $t = t_1$, $t = t_2$ etc., it is decided for each time step whether grid convergence, oscillatory convergence or divergence is obtained, and the uncertainty is estimated, if possible. As shown later, a mix of converging, oscillatory and diverging conditions were found. One of the reasons is that the applied refinement ratio is fairly small which means that the changes between solutions become small. This influences the convergence ratio, i.e. the ratio between the solution changes between grids, which sometimes becomes ill-defined in cases where the solution changes become zero. To study the influence of time step and vertical position of center of gravity, two cases were investigated: one case where the time step was set to half the size used for the grid study, and one case where the vertical position of the center of gravity was moved a distance of 30 % of the draft. The two latter investigations were made with the coarse grid. The results of the verification are described in connection with the CFD results.

5 Results for EFD and CFD

The results presented below cover both measured (EFD) and calculated (URANS and Potential; in general CFD) data. For the EFD results, focus is placed on the global

quantities, i.e. on the resistance and motions of the model in order to study the influence of Froude number, wave length and encounter frequency on the response and resistance of the ship plus the added resistance in waves. The CFD study covers verification of the numerical method plus a comparison of the calculated quantities with the measured data but also a brief discussion of the flow field around the model.

It should be noted that focus is placed on 0th and 1st order terms for the forces and motions since these are the quantities used for calculation of the transfer functions and the added resistance. However, a study of the measured higher order terms showed that for heave and pitch motions, the 2nd and 3rd order amplitudes constitute 0–6 and 0–3 % of the 1st order amplitude, respectively, for the considered conditions. For the resistance in waves, higher order effects are observed since 2nd and 3rd order amplitudes go up to 50 and 15 % of the 1st order amplitude, respectively, for most conditions. More details on the higher order terms can be found in Otzen and Simonsen [23].

5.1 EFD results

5.1.1 Uncertainty assessment

The uncertainty assessment results for the static calm water resistance test are presented in Table 6, and the uncertainty assessment for the dynamic resistance test in waves is presented in Table 7.

Both tables include the bias components of the measured force, the bias $B_{X'}$, the precision limit $P_{X'}$ and total uncertainty $U_{X'}$ expressed in percentage contribution.

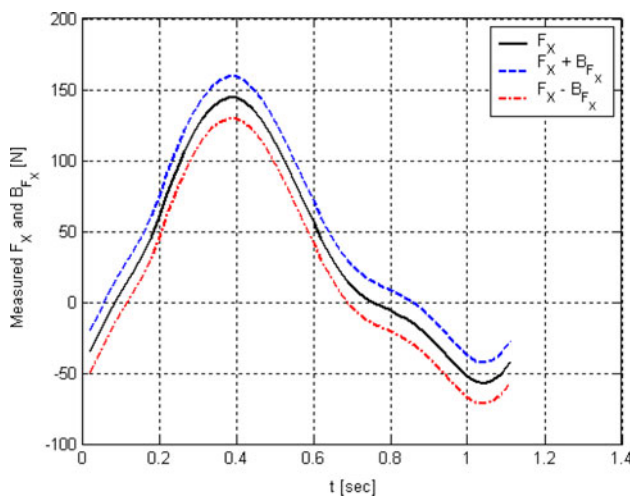
As seen in Table 7, the surface elevation is considered an error contribution to the measured force besides the more obvious bias errors. Each run during the tests was started approximately 160 m from the wave maker, i.e. at a point where the wave height was approximately 10 % lower than the stationary value measured 30 m from the wave maker according to the performed decay test. The error due to uncertainty of the surface elevation was found

Table 6 UA for calm water resistance tests

Term	Fr = 0.26	Fr = 0.33	Fr = 0.40
$B_{\text{calib}, F_{X, \text{meas}}}^2$ in % of $B_{F_{X, \text{meas}}}^2$	42.21	35.60	27.58
$B_{\text{acquis}, F_{X, \text{meas}}}^2$ in % of $B_{F_{X, \text{meas}}}^2$	57.79	64.40	72.42
$B_{X'}$ in % of $U_{X'}^2$	99.07	99.61	99.57
$P_{X'}$ in % of $U_{X'}^2$	0.93	0.39	0.43
X' [–] (mean)	0.0013	0.0018	0.0024
$U_{X'}$ in % of X'	5.83	4.17	3.48

Table 7 UA for wave resistance tests

Fr = 0.26	Resistance
$B_{\text{calib}, F_{X, \text{meas}}}^2$ in % of $B_{F_{X, \text{meas}}}^2$	0.88
$B_{\text{acquis}, F_{X, \text{meas}}}^2$ in % of $B_{F_{X, \text{meas}}}^2$	1.69
$B_{\text{sc}, F_{X, \text{meas}}}^2$ in % of $B_{F_{X, \text{meas}}}^2$	88.00
$B_{\text{t}, F_{X, \text{meas}}}^2$ in % of $B_{F_{X, \text{meas}}}^2$	9.43
$F_{X, \text{meas}}$ [N] (max)	144.36
$B_{F_{X, \text{meas}}}$ in % of $F_{X, \text{meas}}$	10.25
$B_{X'}^2$ in % of $U_{X'}^2$	98.90
$P_{X'}^2$ in % of $U_{X'}^2$	1.10
X' [–] (max)	0.0268
$U_{X'}$ in % of X'	13.58

**Fig. 6** Measured force and its bias limit

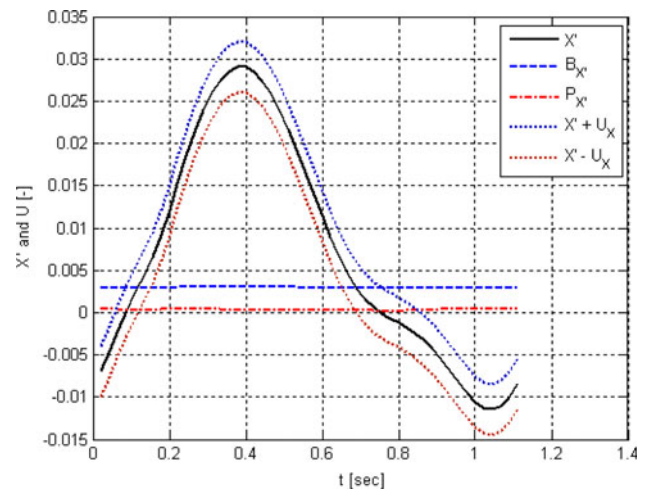
to contribute with just below 90 % of the total bias limit of the force, explaining why the uncertainties of the dynamic tests in waves were somewhat higher than those of the static tests in calm water, presented in Table 6.

The second contribution to the bias limit is the uncertainty of the time at which the data was measured covering just below 10 % of the total bias limit. The last two components are negligible compared to the contribution from the surface elevation and the time.

The uncertainty band for the mean period of the measured force and hydrodynamic force is presented in Figs. 6 and 7, respectively. The contributions of the bias $B_{X'}$ and the precision limit $P_{X'}$ are presented in Fig. 7.

The statistical convergence using both approach I and II for the measured force, the heave and the pitch time series is presented in Table 8.

a_0 is the FS mean value, and a_1 is the first-order amplitude. It is seen that the level of statistical convergence

**Fig. 7** X' including the uncertainty**Table 8** Statistical convergence for $F_{X, \text{meas}}$, heave and pitch

	$F_{X, \text{meas}}$	x_3	x_5
Δ_{SC}	0.263	1.10E–04	5.77E–03
$\Delta_{\text{HSC}}(a_0)$	0.027	6.10E–06	3.31E–04
$\Delta_{\text{HSC}}(a_1)$	0.132	2.40E–05	1.24E–03
Mean values	35.253	0.007	–0.064
$\Delta_{\text{SC}}/\text{mean}(\%)$	0.747	1.641	–9.037
$\Delta_{\text{HSC}}(a_0)/\text{mean}(\%)$	0.077	0.087	–0.517
$\Delta_{\text{HSC}}(a_1)/\text{mean}(\%)$	0.373	0.350	–1.901

for II was smaller for I. However, this makes sense since the signals are harmonic functions for which a traditional running mean takes longer to converge compared to the harming approach in II. However, whether approach I or II is used, the amplitudes of the running means were found to be within the uncertainty bands of the measured quantities, indicating that the level of statistical convergence of the signals was sufficient. In Figs. 8 and 9, the statistical convergence using approach I and II, respectively, has been illustrated for the measured force from one of the repeated runs in the resistance test with waves.

5.1.2 Fourier analysis

The mean periods of the signal were evaluated by approximating 3rd-order Fourier series expansions to the raw signal. As an example, the FS of the measured force signal for a few periods is presented in Fig. 10.

5.1.3 Transfer functions, phases and added resistance

The heave and pitch transfer functions (TF_{x3} and TF_{x5}) and phases (γ_3 and γ_5) versus the λ/L_{pp} are presented in Fig. 11.

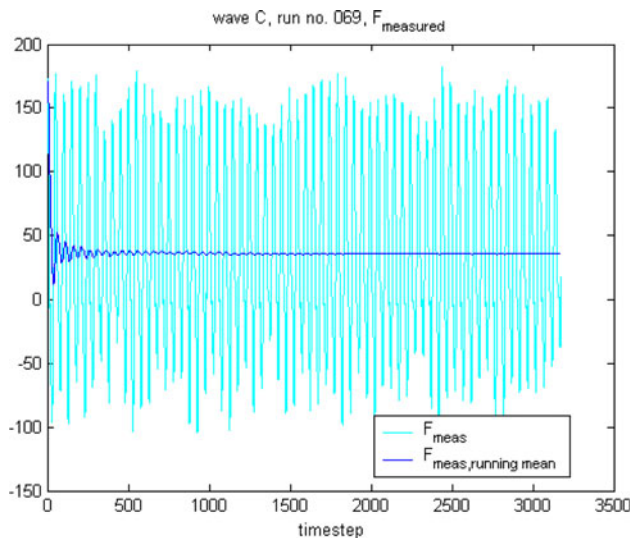


Fig. 8 Statistical convergence I—running mean of signal

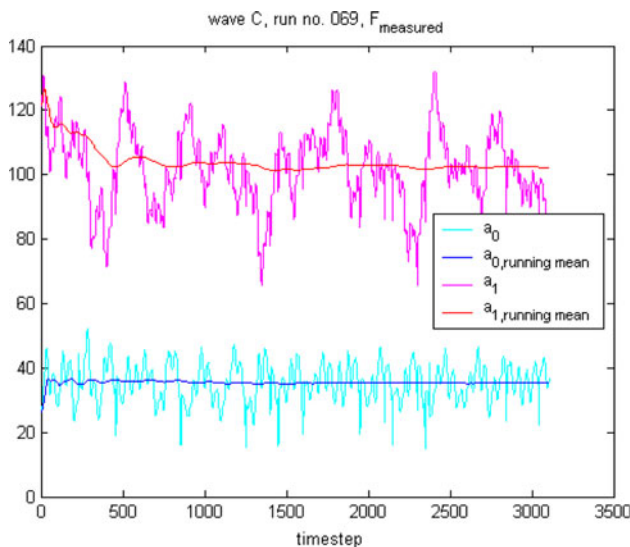


Fig. 9 Statistical convergence II—running mean of FS amplitudes

The heave transfer function TF_{x3} in Fig. 11a and c shows, as expected, a dependency on the wave length and frequency of encounter. Maximum heave response for all three speeds occurred at resonance, and the response increased with speed so that the maximum occurred at $Fr = 0.40$. The global maximum occurred at the highest speed and at a wave length longer than $\lambda/L_{pp} \sim 1.33$, i.e. in accordance with the investigations in Sadat-Hosseini et al. [22].

For TF_{x5} in Fig. 11b and d, the maximum pitch response for all three speeds occurred at an encounter frequency lower than resonance, as observed in Irvine et al. [21], and the response increased with speed. The global maximum occurred at the highest speed. At fixed $\lambda/L_{pp} \sim 1.33$, the maximum response occurred at the lowest speed, i.e. not

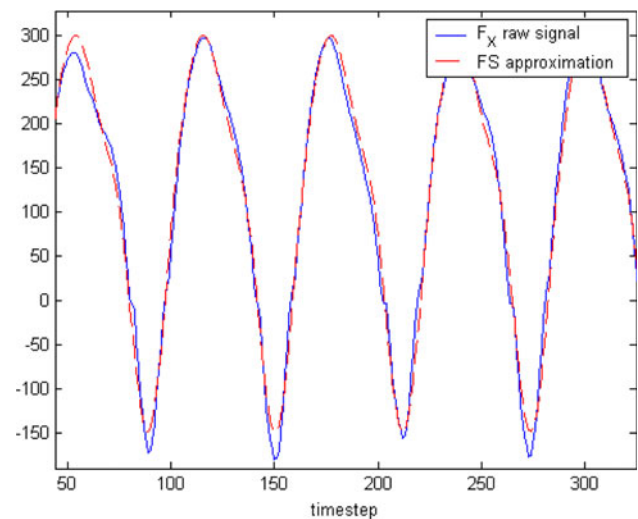


Fig. 10 FS approximation of the measured force

where $f_e \sim f_n$, which deviates from Irvine et al. [21] and Sadat-Hosseini et al. [22]. The phases follow the typical trends for heaving and pitching ships, i.e. the heave phase in Fig. 11e tends to go towards zero in long waves indicating that the heave motion becomes synchronized with the wave motion and the pitch phase presented in Fig. 11f tends to go towards -90 degrees for increasing wave length, i.e. maximum positive pitch one quarter of an encounter period after the wave trough has passed amid-ships. This makes sense since the pitch angle for long waves follows the slope of the wave which is maximum a quarter of a period after wave top.

In Fig. 12, the added resistance for all Froude numbers is plotted. The peak values of the added resistance was observed around $\lambda/L_{pp} \sim 1.33$ and $f_e \sim f_n$. The maximum added resistance was observed were the $\lambda/L_{pp} \sim 1.33$ and $f_e \sim f_n$ conditions coincide, i.e. at the medium speed.

5.2 CFD results

5.2.1 Flow field

The field quantities are briefly discussed for the resonance condition at $Fr = 0.26$. Figure 13 shows the periodic wave pattern which consists of the incoming regular waves and the waves generated by the ship. The wave pattern is shown for quarter periods of one period of encounter. At $t/T_e = 0$, the bow of the ship is located in the middle of the wave crest.

With $\lambda/L_{pp} = 1.15$, the wave length is close to the length of the ship so the stern region is also in a wave crest, and the mid-ship section “hangs” in the wave trough. During the period of encounter, the bow region experiences the most dramatic changes. At $t/T_e = 0$, the bow is deeply

Fig. 11 Transfer functions (left-hand side) and phases (right-hand side) for heave and pitch as function of wave length

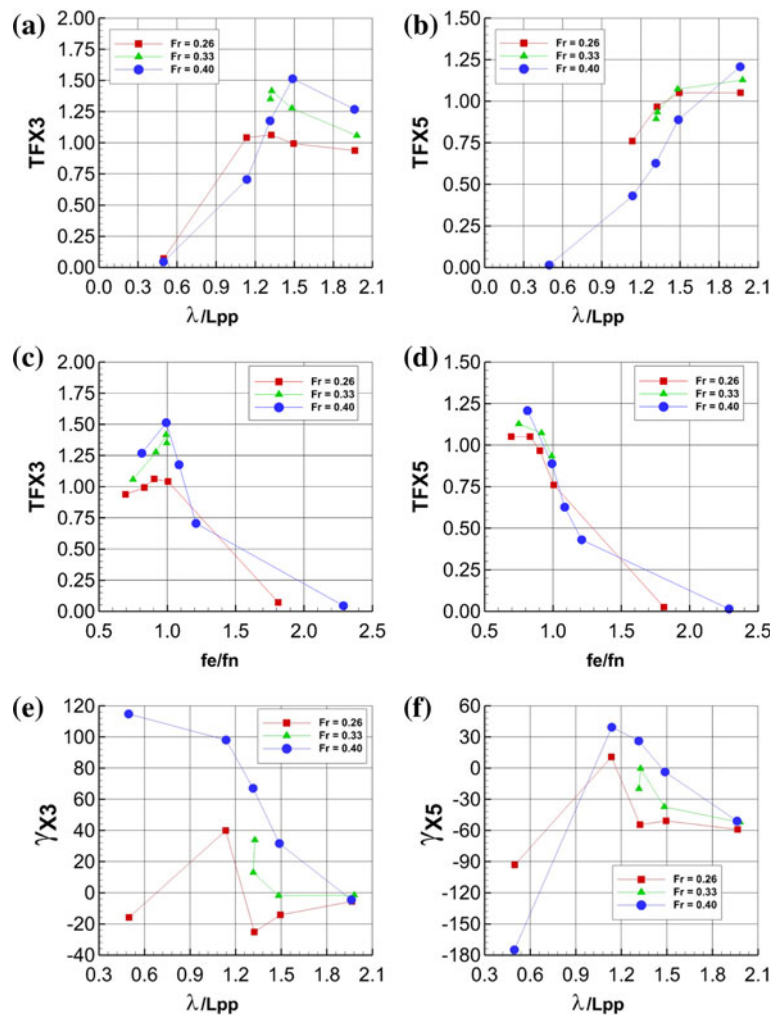
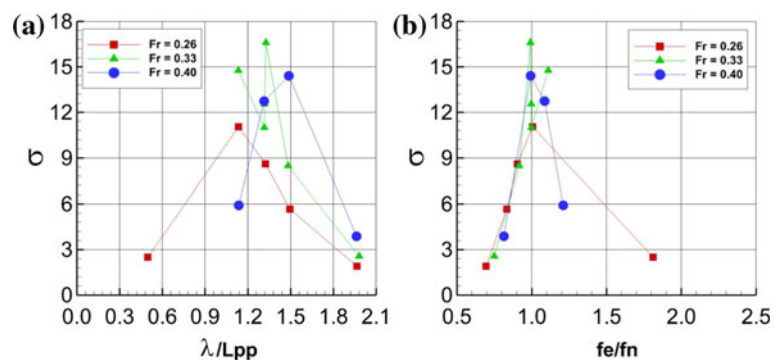


Fig. 12 Added resistance as function of wave length



submerged in the wave, and the flare of the ship generates a wave on top of the incoming wave. As the wave moves on, $t/T_e = 1/4$, the bow starts to come out of the water again, and the wave formation is reduced in this region. At $t/T_e = 1/2$, the bow reaches the wave trough, and most of the fore ship including the bulbous bow comes out of the water which reduces the wave making of the ship. After this, the new wave is coming in towards the bow, $t/T_e = 3/4$, which starts to dive into the wave where the

flared shape again starts to generate waves around the fore body. Then as $t/T_e = 1$ is reached, the periodic behavior of problem leads to a wave pattern similar to $t/T_e = 0$.

Figure 14 shows the axial velocity contours at propeller plane, i.e. $x/L_{pp} = 0.983$. The wake field behind a ship in waves is more complex than in calm water. The figure shows that the combination of the ship motion and the wave changes the shape of the wake field throughout the period of encounter. The resulting wake contours are

Fig. 13 Free surface elevations over one period of encounter, T_e

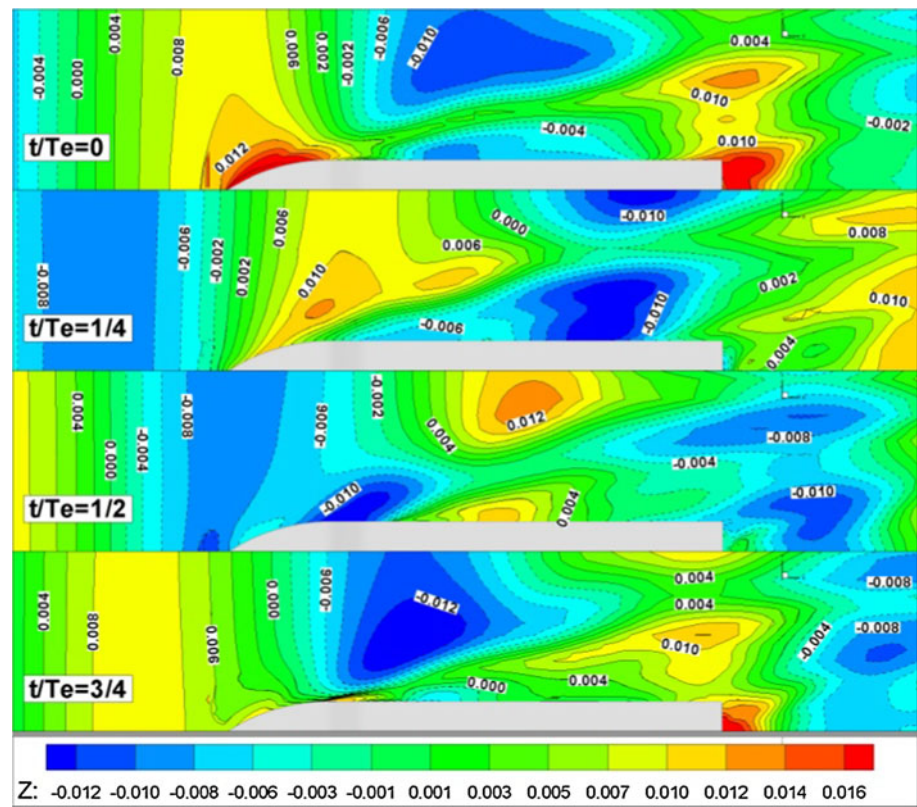


Fig. 14 Axial velocity contours at propeller plane over one period of encounter, T_e

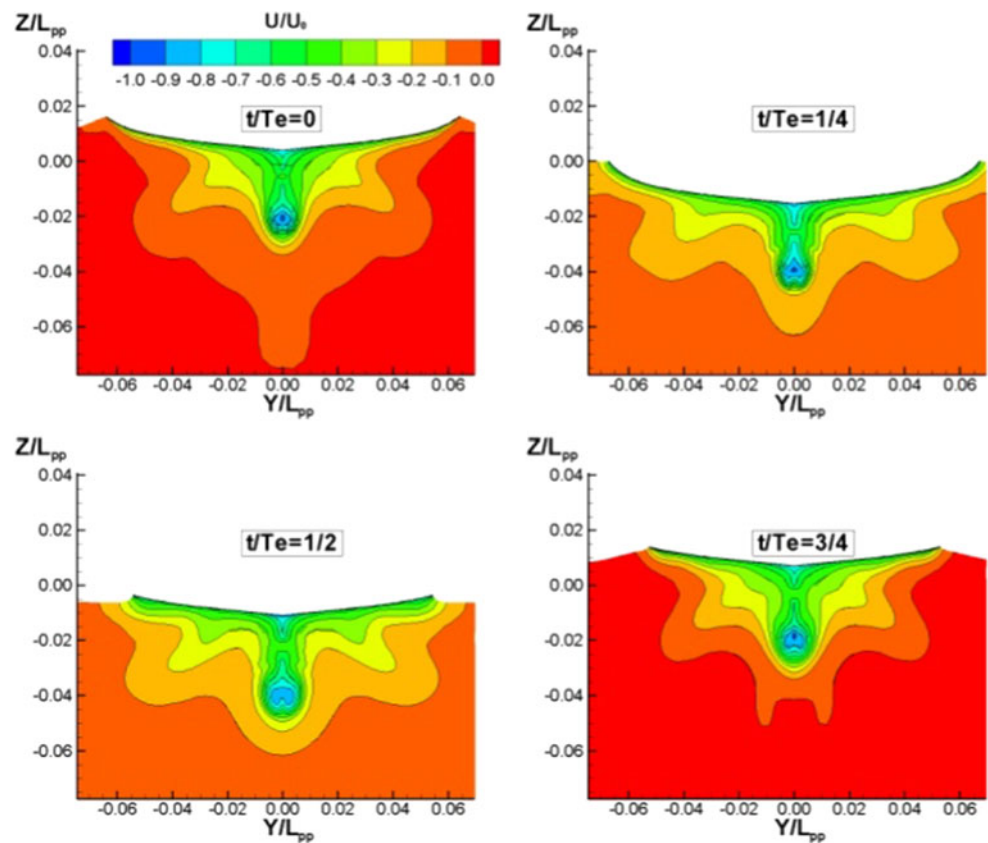
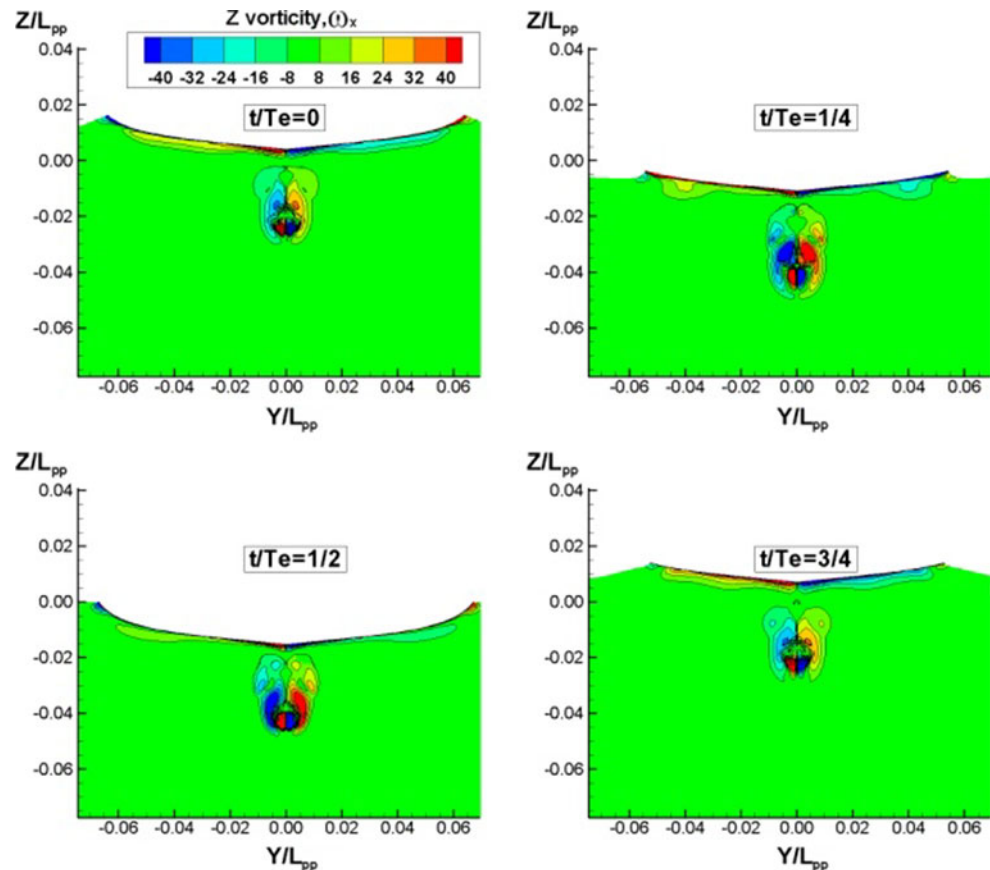


Fig. 15 Axial vorticity contours at propeller plane over one period of encounter, T_e



“squeezed” towards the hull and center plane as the wave crest passes while the contours are “expanding” when the water retreats in the wave trough. The complex wake field is a combination of the normal wake deficit behind the ship, the orbital velocities in the wave and the relatively strong fluctuations in the stern region pressure.

Figure 15 illustrates the axial vorticity distribution in the same cross section. The figure shows the location and the strength of the bilge vortices observed behind the ship. When the stern was located in the wave crest, the extension of the regions with high vorticity were smaller than when the stern was in the wave trough. Further, the bilge vortices were getting somewhat stronger when the stern was in the trough region. As for the wake field, the complex shape of the vortices was a combination of the hull form, ship motion and orbital velocities in the wave.

The last field quantity is the pressure distribution on the hull surface. Figures 16 and 17 show the pressure on the wetted part of the stern and bow, respectively. In the stern, it is characteristic that the pressure increases when the wave crest passes while it decreases in the trough. Figure 17 shows that the portion of the ship being in the water varied a lot over the period of encounter. The bow experienced the largest changes compared to the stern. The pressure variations over the period of encounter were also

significant. The pressure was found to increase, primarily due to stagnation, when the bow dove into the wave. The result of the large changes in pressure and wetted surface area is reflected in the resistance which varies significantly throughout the period of encounter. This is discussed in connection with the integral quantities.

5.2.2 Verification of integral quantities

The computational method was verified based on three systematically refined grids. A study of the grid convergence for the time series for resistance, heave position and pitch angle, seen in Figs. 18, 19 and 20, shows a combination of converging, oscillatory and diverging conditions.

The relatively small refinement ratio leads to quite small changes between grids which may explain the convergence difficulties. Consequently, it is not possible to use Richardson extrapolation for the grid uncertainty estimate or to perform a traditional quantitative verification. Instead the maximum change between grids Δ_G over the considered period of time is used. The results are summarized in Table 9.

As with the EFD time series, the statistical convergence was also checked for the CFD time series using approach I. The running mean for the last two periods of encounter can

Fig. 16 Pressure distribution on the underwater after part of the hull over one period of encounter, T_e

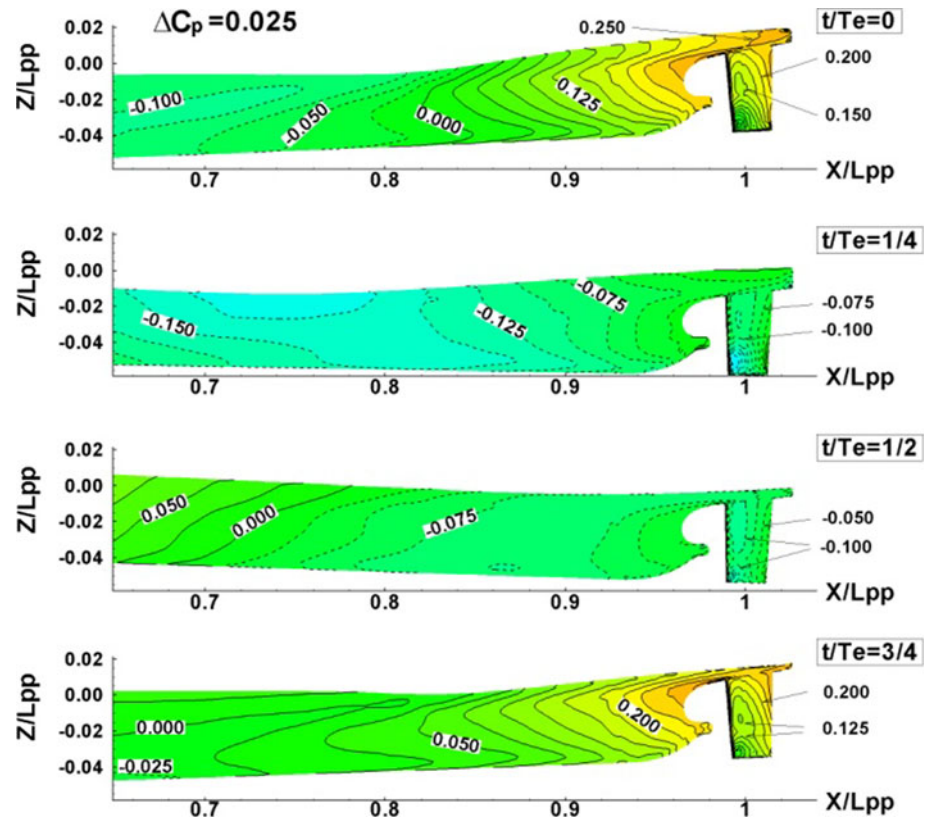
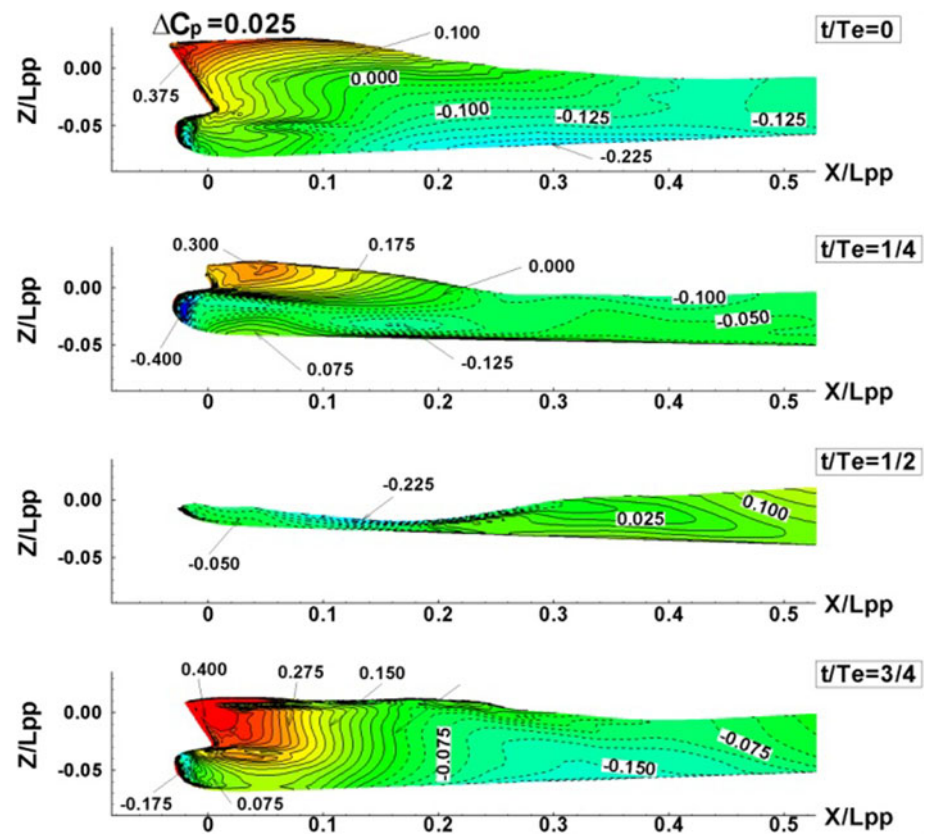


Fig. 17 Pressure distribution on the underwater fore part of the hull over one period of encounter, T_e



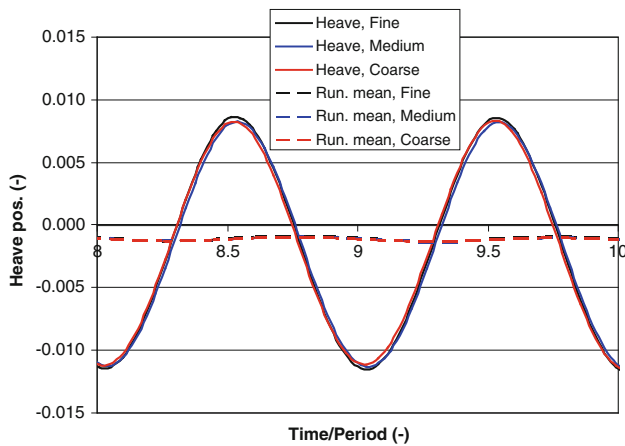


Fig. 18 Calculated heave position from grid study. Time is non-dimensionalized with period of encounter

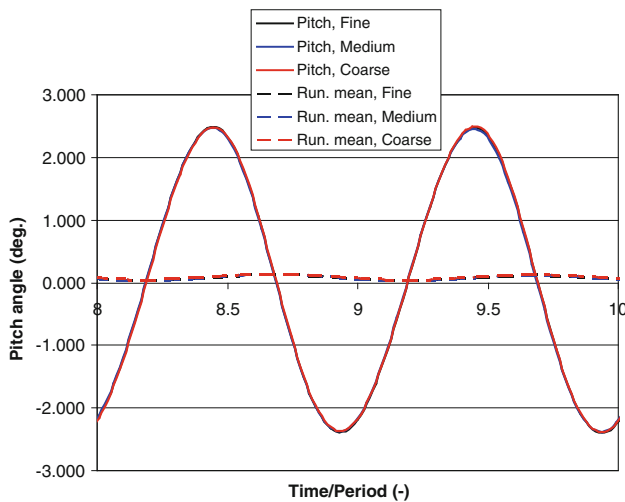


Fig. 19 Calculated pitch angle from grid study

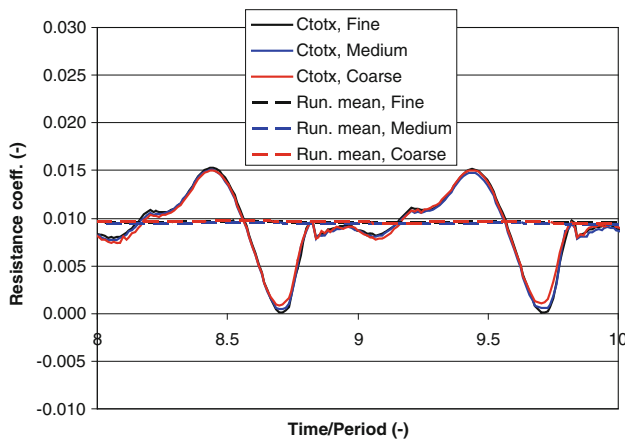


Fig. 20 Calculated resistance coefficients from grid study

Table 9 Grid uncertainty and statistical convergence

Fr	Heave	Pitch	Resist.
Δ_G	0.00089	0.0645	0.00028
Δ_{SC}	0.00038	0.0901	0.00022
Δ_G/S_U (%)	10.3	2.6	1.5
Δ_{SC}/S_U (%)	4.4	3.6	1.4

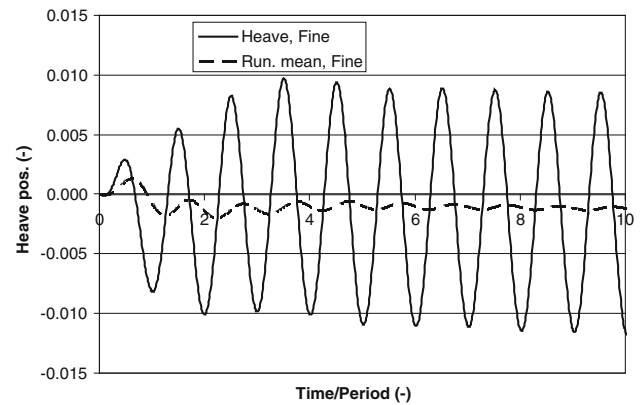


Fig. 21 Running mean for heave over 10 periods of encounter

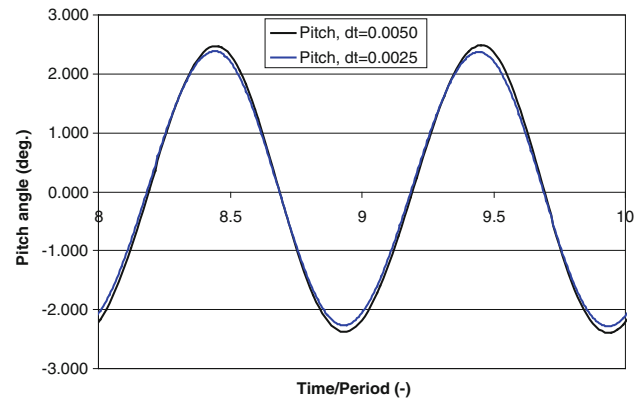


Fig. 22 Pitch angle calculated with different time steps

be seen in Figs. 18, 19 and 20, and it is seen that small oscillations are present. Figure 21 shows the complete time series for heave, and it is seen that the oscillations tend to decay as time passes. In order to improve the statistical convergence and reduce the oscillations further, the simulation could be run longer. Table 9 shows the difference Δ_{SC} between the maximum and minimum values of the oscillations. It is seen that the grid uncertainty and the statistical convergence are of the same order of magnitude.

The effect of time step was also studied. Due to the relatively small changes between grids, the coarse grid was used for this to speed up the computational time. The grid study was done with $dt = 0.005$. The time step check was run with $dt = 0.0025$. Figure 22 shows the calculated pitch

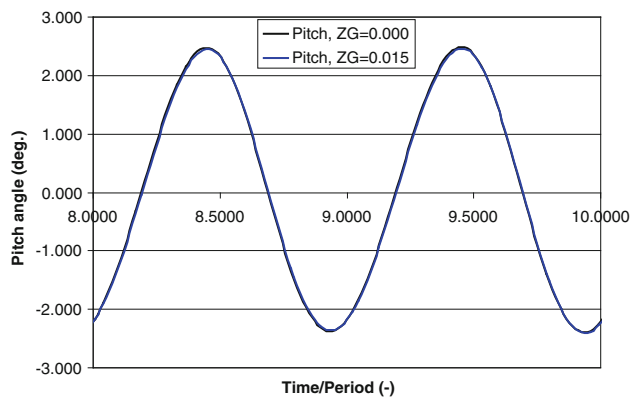


Fig. 23 Pitch angle calculated with different VCG

angle. The amplitudes are slightly reduced while the phase seems to be the same. The same behavior is observed for heave and resistance.

Finally, the sensitivity of the position of the vertical center of gravity was studied by moving VCG upwards as described earlier. Figure 23 shows the calculated pitch angle, and it is seen that the effect is very limited. This was expected since the position of VCG is less important for pitch compared to for instance roll which is not considered in this work. The same behavior is observed for heave and resistance. It should be noted that a sensitivity study of the pitch moment of inertia could also be interesting. But, due to time limitations of the work, it was not done.

5.2.3 Discussion of forces and motions

The results for the integral quantities are presented in terms of zero and first order terms. All quantities are given in earth-fixed coordinates. Finally, the streaming is also calculated, i.e. the differences between calm water values and mean values, i.e. zero order terms, from the wave case

$$\Delta C_i = C_{iWave} - C_{iCalm}. \quad (31)$$

Table 10 shows the calm water resistance coefficient non-dimensionalized according to (3), the dynamic sinkage non-dimensionalized with L_{pp} and the trim angle in degrees. It is seen that CFDSHIP-IOWA captures all values within a range of 3.5–6.9 % of the measured data. For comparison, Table 10 also shows that Star-CCM+ predicts the quantities within 2.6–9.5 %.

For the wave cases, it should be noted that the CFD calculations were done with the nominal wave parameters from Table 2, but the wave parameters for the measured wave ended up being slightly different, shown in Table 11. The different waves will influence the comparison between EFD and CFD when the quantities are compared directly. However, for the non-dimensionalized heave and pitch transfer functions and the added resistance coefficient, the

Table 10 Calm water results

	$X' (-)$	x_{30}/L_{pp}	$x_{50}(\text{deg})$
Fr = 0.26			
EFD	0.00431	−0.0021	−0.1853
CFDSHIP-IOWA	0.00407	−0.0020	−0.1780
Diff	−5.6	−6.4	−4.0
STAR-CCM+	0.00442	−0.0019	−0.1800
Diff	2.6	−9.5	−2.9
Fr = 0.33			
EFD	0.00625	−0.0036	−0.0913
CFDSHIP-IOWA	0.00582	−0.0034	−0.1078
Diff	−6.9	−5.7	18.0
Fr = 0.40			
EFD	0.00798	−0.0047	0.2000
CFDSHIP-IOWA	0.00771	−0.0048	0.1869
Diff	−3.5	3.4	−6.5

Diff is in % of EFD

Table 11 Wave parameters

	ζ_1/L_{pp}	H/λ
EFD	0.00955	1/63.21
CFDSHIP-IOWA	0.00985	1/60.00
Diff	3.1	5.1

Diff is in % of EFD

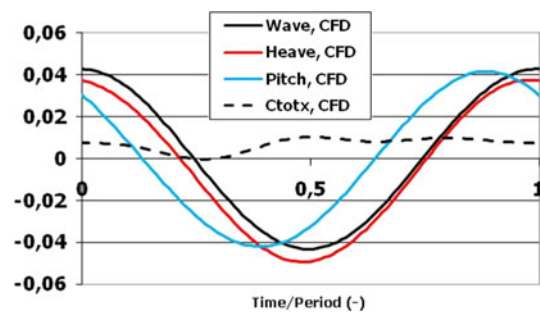


Fig. 24 Heave, pitch, wave elevation and absolute resistance from CFD

wave height is included in the non-dimensionalization which will account for the difference.

Figures 24 and 25 show the calculated and measured time series of the wave elevation in meters at midship position, the heave position in meters, the pitch angle in degrees and the absolute resistance C_{totX} non-dimensionalized according to (3). Resonance condition $Fn = 0.26$, $f_e = f_n = 0.9$ Hz, $\lambda/L_{pp} = 1.15$ is considered, and time is non-dimensionalized with the period of encounter.

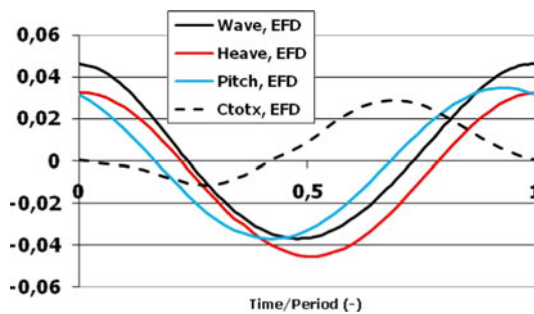


Fig. 25 Heave, pitch, wave elevation and absolute resistance from EFD

Table 12 1st order phase shifts relative to wave

	$\gamma_{X3,1}$ (deg/s)	$\gamma_{X5,1}$ (deg/s)	$\gamma_{TX,1}$ (deg/s)
EFD	6.8	−21.0	−107.4
CFDSHIP-IOWA	−4.1	−39.0	−95.5

The time series of the wave elevation and the motions show a harmonic behavior. The heave position tends to follow the wave elevation but is slightly phase shifted. The pitch signal has the same shape, but the phase shift is larger. Concerning the size of the phase shift, Table 12 shows the 1st-order phase shift of the signals compared to the incoming wave from measurement and from CFD. It is seen that the heave is close to being in phase with the wave, but also that phase shifts have opposite signs. For the pitch angle, the phase shifts have similar signs, but CFD predicts a larger shift than EFD. It is difficult to say exactly why the phase shifts are different, but one explanation could be the different setups between EFD and CFD models, i.e. two posts mounting versus one towing point, which could possibly influence the stiffness and the dynamic behavior of the system. The setups are discussed in further detail below. For the resistance, the shapes of the calculated and measured curves are different, and secondly the amplitudes of the two signals are quite different. Finally, the resistance is phase shifted with approximately 100 degrees compared to the wave according to Table 12. Both EFD and CFD give approximately the same level with a slight underprediction by the calculation.

The transfer functions for heave and pitch, TF_{X3} and TF_{X5} , and the mean levels for heave and pitch motion x_{30}/L_{pp} and x_{50} are given in Table 13 for all computed conditions. For TF_{X3} , the deviations between EFD and RANS CFD are in the range from 4.7 to 14.2 %. For TF_{X5} , the range is 1.2–23.2 %. When it comes to the calculated and measured mean levels for heave and pitch, the deviations range from 13.8 to 47.9 % and from 3.2 to 51.2 %, respectively. There is no clear trend for over and under prediction by CFD. In agreement with the EFD results,

CFD predicts maximum response for TF_{X3} at the resonance condition at high speed, i.e. $Fr = 0.40$, $f_e = f_n = 0.89$ Hz, $\lambda/L_{pp} = 1.50$. For TF_{X5} , CFD predicts the maximum at $Fr = 0.40$, $f_e = f_n = 0.89$ Hz, $\lambda/L_{pp} = 1.50$, while EFD predicts it at $Fr = 0.26$, $f_e = 0.81$ Hz, $\lambda/L_{pp} = 1.33$. However, the TF_{X5} values are in both cases pretty close and within the uncertainties of the CFD and EFD.

For the total resistance, Table 13 shows the 0th and 1st harmonic of the resistance time series. 0th harmonic is predicted fairly well compared to the measurement, and CFD predicts maximum at $Fr = 0.40$, $f_e = f_n = 0.89$ Hz, $\lambda/L_{pp} = 1.50$ which is in agreement with the EFD results. The 1st harmonic is somewhat underpredicted by the RANS code. The reason for the large difference may be found in the way the model was towed in EFD and CFD. In the experiment, the model was mounted in two trim holders or posts connected to the model via two gauges. The posts were designed so they can move up and down with the heaving and pitching model. Further, one was fixed in surge to carry the main load while the other was free to move in surge. However, the system was not completely stiff which means that it may have allowed small surge motions of the model. Further, the free gauge, which ideally should move freely, may not have been able to do so in reality due to friction in the system. This may have introduced some additional residual force internally in the system while the ship was heaving and pitching, and it could be reflected in the instantaneous resistance signal as higher amplitude. The system is primarily designed for measurement of the mean resistance in order to determine the added resistance, so the effect of the larger amplitudes is believed to be reduced in the averaging. In the CFD setup, the model was towed in an ideal stiff setup which was locked in surge. Consequently, the shape of the time series for the resistance obtained with the different systems may be different, and it may not be possible to compare the two signals directly at a given instant of time. The average level of resistance should, however, be fine, and it should be possible to compare the measured and calculated mean resistance. It should also be mentioned in this connection that the total resistance is non-dimensionalized according to (3) which means that the difference in wave heights between EFD and CFD will influence the comparison. However, it does not explain the large 1st-order difference.

To make an additional check of the calculated amplitudes, an additional computation was made independently with the commercial RANS code Star-CCM+. It is seen that these results also show the underprediction of the 1st-order amplitude of resistance. This trend was further shown at the CFD Workshop in Gothenburg 2010 where additional RANS computations with four different codes were conducted for the $Fn = 0.26$ case. Based on the conclusions in Stern et al. [34], all the CFD codes are found to

Table 13 Transfer functions and mean values and resistance coefficients

	x_{30}/L_{pp}	TF_{x3}	x_{50} (deg)	TF_{x5}	X'_0	X'_1
$Fn = 0.26, f_e = f_n = 0.90$ Hz, $\lambda/L_{pp} = 1.15$						
EFD	−0.00124	0.950	−0.065	0.693	0.00702	0.01761
CFDSHIP-IOWA	−0.00109	0.995	−0.036	0.769	0.00686	0.00370
<i>Diff</i>	−13.8	4.7	−44.6	11.0	−2.3	−79.0
STAR-CCM+	−0.00163	0.861	−0.083	0.731	0.00610	0.00487
<i>Diff</i>	31.5	−9.4	27.7	5.5	−13.2	−72.3
$Fr = 0.26, f_e = 0.81$ Hz, $\lambda/L_{pp} = 1.33$						
EFD	−0.00154	1.107	−0.012	0.971	0.00773	0.02343
CFDSHIP-IOWA	−0.00196	0.950	−0.011	0.959	0.00714	0.01020
<i>Diff</i>	27.6	−14.2	−8.1	−1.2	−7.7	−56.5
$Fr = 0.33, f_e = f_n = 0.89$ Hz, $\lambda/L_{pp} = 1.33$						
EFD	−0.00278	1.361	0.067	0.896	0.00874	0.03524
CFDSHIP-IOWA	−0.00411	1.286	0.069	0.948	0.00780	0.00380
<i>Diff</i>	47.9	−5.6	3.2	5.8	−10.8	−89.2
$Fr = 0.40, f_e = 0.98$ Hz, $\lambda/L_{pp} = 1.33$						
EFD	−0.00458	1.202	0.550	0.634	0.01002	0.03245
CFDSHIP-IOWA	−0.00551	1.242	0.268	0.781	0.00871	0.00453
<i>Diff</i>	20.4	3.3	−51.2	23.2	−13.1	−86.0
$Fr = 0.40, f_e = f_n = 0.89$ Hz, $\lambda/L_{pp} = 1.50$						
EFD	−0.00469	1.571	0.431	0.951	0.01033	0.03811
CFDSHIP-IOWA	−0.00633	1.392	0.517	0.976	0.00894	0.00434
<i>Diff</i>	34.9	−11.4	19.8	2.7	−13.5	−88.6

Diff is in % of EFD

agree reasonably well with the measured 0th harmonic resistance component, but when it comes to the 1st harmonic of the resistance, they all underpredict it in the same manner as observed in the present work.

As mentioned above, the streaming was calculated. The streaming of the resistance is particularly interesting because it represents the added resistance in waves. Table 14 summarizes the results. The largest deviations are seen for the heave streaming, but this quantity is quite small and difficult to predict accurately with the “noise” in both experiment and CFD. The same applies to the pitch streaming where the largest differences are related to the highest speed. For the added resistance calculated according to (5), the agreement between EFD and CFD is fairly good at the low speed, but as speed is increased, the deviation goes up and ends up being fairly large at the high speed. However, recalling that the underprediction of the average resistance in waves was increasing with ship speed compared to the measurement, it must be expected that the added resistance is most underpredicted for the high speed. It is therefore important to obtain a good prediction of the average resistance in waves if the added resistance is to be predicted well. In the present CFD simulations, the low Froude number CFD settings were used for all calculations. It is possible that a more careful design of the settings and meshes could have improved the mean resistance estimate and thereby the added resistance. In future work, this should be investigated further.

Table 14 Streaming results

	σ_{aw}	$\Delta x_{30}/L_{pp}$	Δx_{50}
$Fn = 0.26, f_e = f_n = 0.90$ Hz, $\lambda/L_{pp} = 1.15$			
EFD	11.049	0.00086	0.120
CFDSHIP-IOWA	11.540	0.00091	0.142
<i>Diff</i>	4.4	6.0	18.0
STAR-CCM+	6.949	0.00027	0.097
<i>Diff</i>	37.1	68.6	19.1
$Fn = 0.26, f_e = 0.81$ Hz, $\lambda/L_{pp} = 1.33$			
EFD	8.617	0.00056	0.173
CFDSHIP-IOWA	9.494	0.00004	0.167
<i>Diff</i>	10.2	−92.9	−3.6
$Fn = 0.33, f_e = f_n = 0.89$ Hz, $\lambda/L_{pp} = 1.33$			
EFD	13.381	0.00082	0.158
CFDSHIP-IOWA	15.294	−0.00071	0.177
<i>Diff</i>	14.3	−186.6	11.7
$Fn = 0.40, f_e = 0.98$ Hz, $\lambda/L_{pp} = 1.33$			
EFD	12.739	0.00012	0.350
CFDSHIP-IOWA	7.319	−0.00071	0.081
<i>Diff</i>	−42.5	−691.7	−76.8
$Fn = 0.40, f_e = f_n = 0.89$ Hz, $\lambda/L_{pp} = 1.50$			
EFD	14.415	0.00001	0.231
CFDSHIP-IOWA	7.078	−0.00153	0.330
<i>Diff</i>	−50.9	−15400.0	42.9

Diff is in % of EFD

Fig. 26 Transfer functions (heave and pitch) and added resistance as function of wave length, $Fn = 0.26$

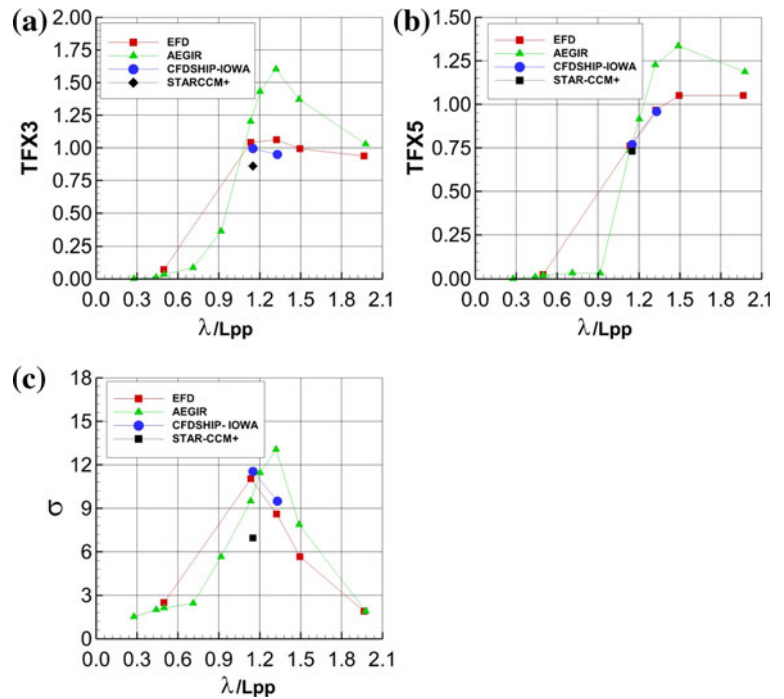
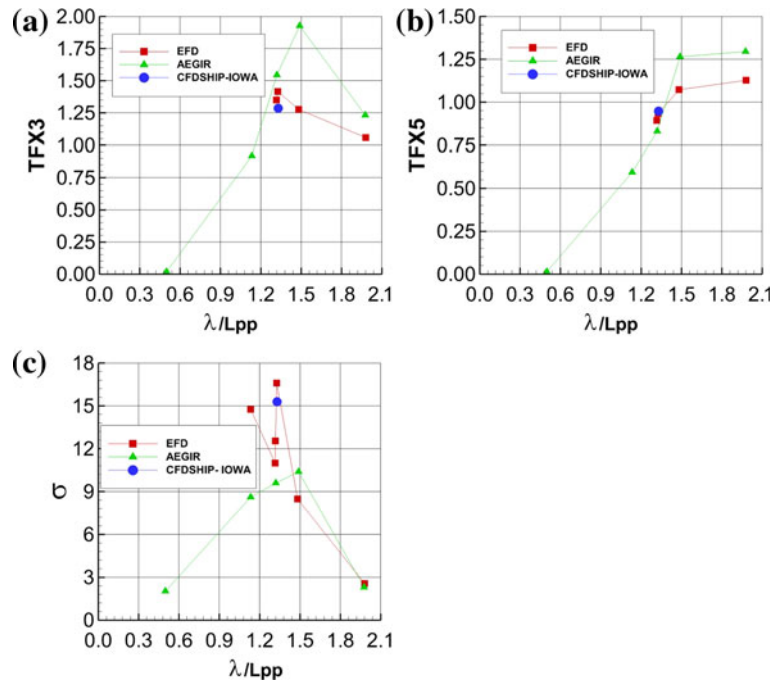


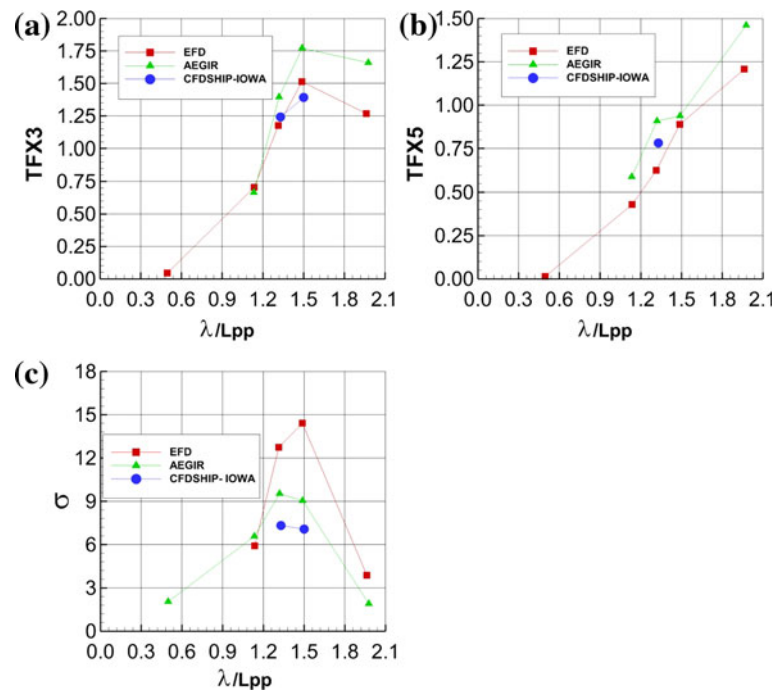
Fig. 27 Transfer functions (heave and pitch) and added resistance as function of wave length, $Fn = 0.33$



Finally, Figs. 26, 27 and 28 show the heave and pitch transfer functions as well as the mean added resistance predicted by EFD, CFDSHIP-IOWA, STAR-CCM+ and AEGIR [6], which is a B-spline based potential code. The motions are better predicted by the CFDSHIP-IOWA code than by the potential code. Generally, AEGIR seems to overestimate the motions for the three speeds. Regarding the mean added resistance, CFDSHIP-IOWA shows better agreement with measurements compared to AEGIR for

the two lowest Froude numbers. At the highest Froude number, both codes seem to underpredict the added resistance. For the single case with STAR-CCM+, the added resistance is underpredicted. However, this is due to the mesh moving technique applied at the time of the simulations. It has later been improved so overset meshes can be applied instead, which should improve the results since the incoming waves are less disturbed. This should be tested in future work.

Fig. 28 Transfer functions (heave and pitch) and added resistance as function of wave length, $F_n = 0.40$



6 Concluding remarks and future work

In the present work, the KCS container ship was investigated in regular head seas by means of EFD and CFD. The experimental study was conducted in FORCE Technology's towing tank in Denmark, and the primary CFD study including verification was conducted using the RANS code CFDSHIP-IOWA. Additional computation was done with the RANS code Star-CCM+ and the potential flow code AEGIR for the sake of comparison. The experiment was designed and conducted in order to study the ship's motion response and added resistance in waves. Three speeds were covered, and the wave conditions were chosen to cover resonance and maximum forcing conditions.

The results from the test cover the ship's heave and pitch positions, the resistance and the wave elevation. The heave transfer function depends on the wave length and frequency of encounter. Maximum heave response for all three speeds occurred at resonance. The response was seen to increase with speed, i.e. global maximum occurred at maximum speed. For fixed $\lambda/L_{pp} \sim 1.33$ where the maximum forcing occurs, the maximum response occurred where $f_e \sim f_n$, i.e. in accordance with coincidence of $\lambda/L_{pp} \sim 1.33$ and $f_e \sim f_n$, but it was not the global maximum. For the pitch transfer function, the maximum response for all three speeds occurred at encounter frequency lower than resonance, and the response increased with speed so global maximum was seen to occur at the highest speed. At fixed $\lambda/L_{pp} \sim 1.33$, the maximum response occurred at the lowest speed, i.e. not at the coincidence condition where $f_e \sim f_n$. The phases followed

the typical trends for heaving and pitching ships, i.e. the heave phase went towards zero in long waves, and the pitch phase went towards -90 degrees for increasing wave length. For the added resistance, the peak value was observed around $\lambda/L_{pp} \sim 1.33$ and $f_e \sim f_n$. The maximum added resistance was observed where the $\lambda/L_{pp} \sim 1.33$ and $f_e \sim f_n$ conditions coincided. So, with respect to the idea of maximum response at the condition where $\lambda/L_{pp} \sim 1.33$ and $f_e \sim f_n$ coincided, added resistance followed this trend for $\lambda/L_{pp} \sim 1.33$, but it was not seen with regard to pitch and heave.

In addition to the measurement itself, the experimental uncertainty was also investigated in connection with the test. The results for the resistance show that in calm water the measurement uncertainty was of the same order of magnitude as for the PMM test setup, i.e. around three percent, as in Simonsen [35]. However, this makes sense since both systems are two-gauge setups. The picture is a little different when it comes to the measurements in waves where the uncertainties increase compared to calm water. The precision limit is relatively small which indicates fairly good repeatability, but the bias error related to the wave elevation seems to be dominant. The result is an uncertainty of around 10 % of the maximum measured resistance.

Concerning the CFD calculations, a study of the flow field reveals a quite complex time-varying flow pattern caused by the combination of the incoming waves, the ship motions and the hull form. The incoming wave pattern was disturbed by the waves generated by the ship as it moved up and down in the water. Large variations were also seen

in the pressure and velocity fields. As the bow moved in and out of the water, the portion of the hull being under water varied significantly which again influenced the pressure field. Actually the bow experienced larger relative motions than the stern. In the wake behind the ship, the axial velocity and vorticity contours also changed drastically throughout the period of encounter as a consequence of the motion of the ship, the pressure changes from the passing wave and the orbital velocities in the wave.

With respect to the comparison between the motions and forces from EFD and CFDSHIP-IOWA, fairly good agreement was found for resistance and dynamic sinkage and trim in calm water. Values were predicted within a range of 3.5 to 6.9 % of measurements. STAR-CCM+ is within the range 2.6–9.5 %. In waves, CFD captured the heave and pitch motions within ranges of 4.7–14.2 and 1.2–23.2 % of measurement, respectively. When the calm water dynamic sinkage and trim are compared with the mean values in waves, the streaming shows that the difference between EFD and CFD increased. However, the streaming values are small quantities that are difficult to predict, particularly since they are easily disturbed by the experimental and numerical uncertainties.

It is more difficult to calculate the absolute resistance, and consequently larger differences were found. The 0th harmonic in waves was predicted reasonably well within a range of 2.3–13.5 % of the measurements with the largest deviations at high speed. The 1st harmonic of the resistance time series was more difficult to capture, and CFD under-predicted the quantity within a range of 56.5–89.2 % of the measurement. The differences cannot be explained by the small differences in wave heights between EFD and CFD. Concerning the phase shifts between the incoming wave and the response, EFD and CFD seem to be in reasonable agreement. When it comes to the added resistance, it was calculated within a range of 4.4–50.9 % of EFD data. Comparisons between RANS computations, potential flow calculations and measurements show that RANS, in most cases, predicts both motions and added resistance better than potential flow.

The observed deviations between measured and calculated 1st harmonic for the resistance cannot be explained by the simulation or measurement uncertainty alone since the uncertainty levels are quite small compared to the difference between the EFD and CFD data. Computations with two different CFD codes from this work and results from the CFD workshop in Gothenburg 2010 all show the under prediction of the 1st harmonic so the reason for the large difference in the amplitude is believed to be found in the way the model is towed. In the experiment, the model was mounted in a two-gauge system via two trim holders while the CFD model was made with a single towing point. For the reasons discussed in the paper, this may have

influenced the shape of the measured and computed resistance time series, contributing to different amplitudes. The measurement system was primarily designed for measurement of the mean resistance in order to determine the added resistance, and based on the presented resistance results it seems that the EFD and CFD resistance signals may not be comparable at a given instant of time. However, the average level of resistance should be fine, and it should be possible to compare the measured and calculated mean resistance.

Finally, the future work should cover more detailed investigations of the difference in the resistance time series between EFD and CFD. It would be interesting to get more EFD data which is measured in a single towing point setup with a stiff connection to the carriage, similar to the one applied in the CFD method. Finally, it would also be interesting to carry out a study of the influence of wave steepness on the ship's response plus a study of the with-propeller conditions to investigate the added powering in waves.

Acknowledgments This research was sponsored by a FORCE Technology, Office of Naval Research (ONR) contract N00014-07-C-0035 and grant N00014-09-1-1055 under the Naval International Cooperative Opportunities in Science and Technology Program (NICOP). Additionally, this work was supported in part by a grant of computer time from the DOD High Performance Computing Modernization Program at NAVO MSRC. Thanks to Pablo Carrica, IIHR for assistance related to code issues.

References

1. Gerritsma J, Beukelman W (1972) Analysis of the resistance increase in waves of a fast cargo ship. *Int Shipp Process* 19:285–293
2. Salvesen N (1974) Second-order steady-state forces and moments on surface ship in oblique regular waves. In: *Symposium on Marine Vehicles*, London, pp 212–226
3. Lee C-H (1995) Wamit theory manual. MIT Technical report, Report No. 95-2., Massachusetts Institute of Technology, Cambridge
4. Bingham HB (1994) Simulation ship motions in time domain. PhD thesis, Massachusetts Institute of Technology, Cambridge
5. Kring D (1994) Time domain ship motions by a three-dimensional Rankine panel method. PhD thesis, Massachusetts Institute of Technology, Cambridge
6. Joncquez SAG (2009) Second-order forces and moments acting on ships in waves. PhD thesis, Technical University of Denmark, Kongens Lyngby
7. Sato Y, Miyata H, Sato T (1999) CFD simulation of 3-dimensional motion of a ship in waves: application to an advancing ship in regular heading waves. *Mar Sci Technol* 4:108–116
8. Hochbaum CA, Vogt M (2002) Towards the simulation of sea-keeping and maneuvering based on the computation of the free surface viscous flow. In: *Proceedings of the 24th Symposium on Naval Hydrodynamics*, ONR, Fukuoka
9. Wilcox DC (1988) Re-assessment of the scale-determining equation for advanced turbulence models. *AIAA J* 26(11): 1299–1310

10. Orihara H, Miyata H (2003) Evaluation of added resistance in regular incident waves by computational fluid dynamics motion simulation using overlapping grid system. *Mar Sci Technol* 8:47–60
11. Weymouth G, Wilson R, Stern F (2005) RANS CFD predictions of pitch and heave ship motions in head seas. *J Ship Res* 49:80–97
12. Carrica PM, Wilson RW, Noack RW, Stern F (2007) Ship motions using single-phase level set with dynamic overset grids. *Comput Fluids* 36:1415–1433
13. Hu C, Kashiwagi M (2007) Numerical and experimental studies on three dimensional water on deck with a modified Wigley hull. In: *Proceedings of the Ninth International Conference in Numerical Ship Hydrodynamics*, Ann Arbor
14. Stern F, Carrica P, Kandasamy M, Ooi SK et al (2008) Computational hydrodynamic tools for high-speed sealift: phase II final report. IIHR Technical Report No. 465, The University of Iowa, Iowa City
15. Wilson RV, Ji L, Karman SL, Hyams DG, Sreenivas K, Taylor LK, Whitfield DL (2008) Simulation of large amplitude ship motions for prediction of fluid–structure interaction. In: *Proceedings of the 27th Symposium on Naval Hydrodynamics*, ONR, Seoul
16. Paik KJ, Carrica PM, Lee D, Maki K (2009) Strongly coupled fluid–structure interaction method for structural loads on surface ships. *Ocean Eng* 36:1346–1357
17. Castiglione T, Stern F, Kandasamy M, Bova S (2009) Unsteady RANS simulations for a catamaran advancing in regular waves. In: *Proceedings Tenth International Conference on Fast Sea Transportation*, Athens
18. Mousaviraad SM, Carrica PM, Stern F (2010) Development and validation of harmonic wave group single-run procedure for RAO with comparison to regular wave and transient wave group procedures using RANS. *Ocean Eng* 37:653–666
19. Simonsen CD, Stern F (2010) CFD simulation of KCS sailing in regular head waves. In: *Proceedings from Gothenburg 2010—A Workshop on Numerical Ship Hydrodynamics*, vol II, Gothenburg
20. Carrica PM, Paik K, Hosseini H, Stern F (2008) URANS analysis of a broaching event in irregular quartering seas. *Mar Sci Technol* 13(4):395–407
21. Irvine M Jr, Longo J, Stern F (2008) Pitch and heave tests and uncertainty assessment for a surface combatant in regular waves. *J Ship Res* 52(2):146–163
22. Sadat-Hosseini H, Wu P-C, Carrica PM, Kim H, Toda Y, Stern F (2012) CFD verification and validation of added resistance and motions of KVLCC2 with fixed and free surge in short and long head waves. Submitted for publication in *Ocean Engineering*
23. Otzen JF, Simonsen CD (2008) Uncertainty assessment for KCS resistance and propulsion tests in waves. FORCE Technology report no. ONRIII187 01, Lyngby
24. Yoon H-S (2009) Phase-averaged stereo-PIV flow field and force/moment measurements for surface combatant in PMM maneuvers. PhD thesis, IIHR, University of Iowa, Iowa city
25. ITTC (1999) Uncertainty analysis in EFD, uncertainty assessment methodology, 4.9-03-01-01. In: *22nd International Towing Tank Conference*, Seoul/Beijing
26. Xing T, Stern F (2008) Factor of safety for Richardson extrapolation for industrial application. IIHR Technical Report No. 469, The University of Iowa, Iowa City
27. Noack R (2005) SUGGAR: a general capability for mowing body overset grid assembly. In: *AIAA paper 2005-5117*, 17th AIAA Computational Fluid Dynamics Conference, Toronto
28. Stokes GG (1847) On the theory of oscillatory waves. *Trans Camb Philos Soc* 8:441–455
29. Star-CCM+ Users Manual, v.7.06 (online version) (2012)
30. Kring DC, Milewski WM, Fine NE (2004) Validation of a NURBS-based BEM for a multihull ship seakeeping. In: *25th Symposium on Naval Hydrodynamics*, St. John's
31. Stern F, Wilson RV, Coleman HV, Paterson EG (2001) Comprehensive approach to verification and validation of CFD simulations-Part I: methodology and procedures. *ASME J Fluids Eng* 124(4):793–802
32. Wilson R, Shao J, Stern F (2004) Discussion: criticism of the “Correction Factor” verification method. *ASME J Fluids Eng* 126:704–706
33. Xing T, Carrica PM, Stern F (2008) Computational towing tank procedure for single run curves of resistance and propulsion. *ASME J Fluids Eng* 130(1):101102
34. Stern F, Sadat-Hosseini H, Mousaviraad M, Bhushan S (2012) Evaluation of seakeeping predictions. In: *Final Proceedings from Gothenburg 2010—A Workshop on Numerical Ship Hydrodynamics*, Chapter 4, vol II, Gothenburg
35. Simonsen CD (2004) PMM model test with DDG51 including uncertainty assessment. FORCE Technology report no. ONRIII187, Lyngby